Correspondence to:
N. Najibi and N. Devineni,
nn289@cornell.edu;
ndevineni@ccny.cuny.edu

Understanding the Spatial Organization of Simultaneous Heavy Precipitation Events Over the Conterminous United States

Nasser Najibi[1,2,3,4] , **Ariel Mazor**[1], **Naresh Devineni**[1,2,3] , **Carolien Mossel**[3,5], and **James F. Booth**[3,5,6]

[1]Department of Civil Engineering, City University of New York (City College), New York, NY, USA, [2]Center for Water Resources and Environmental Research, City University of New York, New York, NY, USA, [3]NOAA/Center for Earth System Sciences and Remote Sensing Technologies (CESSRST), City University of New York, New York, NY, USA, [4]Now at Department of Biological and Environmental Engineering, Cornell University, Ithaca, NY, USA, [5]Department of Earth and Atmospheric Sciences, City University of New York (City College), New York, NY, USA, [6]Program in Earth and Environmental Sciences, Graduate Center, City University of New York, New York, NY, USA

Abstract We introduce the idea of simultaneous heavy precipitation events (SHPEs) to understand whether extreme precipitation has a spatial organization manifested as specified tracks or contiguous fields with inherent scaling relationships. For this purpose, we created a database of SHPEs using ground-based precipitation observations recorded by the daily Global Historical Climatology Network across the conterminous United States during 1900–2014. SHPEs are examined for their seasonality, spatial manifestation, orientation, and areal extent. We quantified the spatial distribution of the centroids and principal axes of SHPEs and their quasi-elliptical manifestations, azimuthal orientations, and areal extents on the ground. Four seasons, December-January-February (DJF), March-April-May (MAM), June-July-August (JJA), and September-October-November (SON) are considered to examine the spatial patterns and associated large-scale atmospheric circulations. Results indicate that there are 54, 58, 103, and 204 SHPEs in DJF, MAM, JJA, and SON seasons, and their longest stretches range on average between 650 and 1,600, between 850 and 1,500, between 950 and 1,550, and between 750 and 1,450 km, respectively. SHPEs in the DJF, MAM, and JJA seasons occur mostly over the Pacific coast and central and midwestern United States, respectively. The atmospheric circulation patterns and mechanisms of precipitable water vapor and moisture transport in the atmosphere are also discussed in relation to these SHPEs. Power laws explain SHPEs' underlying area scaling behavior in all the four seasons, with stronger evidence in DJF and MAM. A seasonal spatial risk model is developed to predict the likelihood of SHPEs. Quantifying the characteristics of SHPEs and modeling their footprints can improve the projections of flood risk and understanding of damages to interconnected infrastructure systems.

Plain Language Summary We present a new approach to quantify extreme regional precipitation considering the spatial structure of extreme events. Defined as simultaneous heavy precipitation events (SHPEs), they measure the central location, spatial extent, and the orientation of widespread heavy rains on the land. These characteristics are derived for four seasons over the entire 20th and early 21st centuries (115 years). We interpret the features of SHPEs over the Pacific Coast, Midwest, and the Northeastern United States using a combination of atmospheric circulation and moisture transport features. A seasonal spatial risk model is also developed to identify the probability of any region experiencing SHPEs. The framework and findings presented in this study can help in developing improved flood risk management methods by public/private planners and agencies. The database can be used by the Earth system scientists working on extreme events to explore new avenues of research.

1. Introduction

1.1. Motivation

Simultaneous heavy precipitation over a region creates rapid inundation and significant risk of flooding. It imposes a threat to the socioeconomic conditions and environment by causing severe damage to interconnected infrastructure systems and suspension of services over extended territories. The 1993 summer

flooding known as the "Great USA Flood of 1993" along the Mississippi watershed and all over the U.S. Midwest is one such example. According to Mo et al. (1995), a combination of geographic features and mesoscale processes has caused this "Great USA Flood of 1993." They showed that the orientation of the Rocky Mountains which kept a leeward trough over their eastside, strong westerly eddies which caused an anomalous upper-level zonal wind flow, and an active low-level jet (LLJ) which transported tropical moisture to the Great Plains were the critical factors in causing widespread extreme rainfall. There were uniquely repetitive and large aerial extent heavy rainstorms from May to August 1993 that bombarded the central United States and Upper Midwest. Ultimately, such widespread extreme rain combined with preceding wet soil conditions caused significant flooding across North Dakota, South Dakota, Nebraska, Kansas, Minnesota, Iowa, Missouri, Wisconsin, and Illinois with $15 billion (U.S. dollars) in damages. The system of railroad transportation in the Midwest was halted, thousands of levees along the Missouri and Mississippi Rivers failed, and more than 60,000 km^2 of farmland and many water treatment plants were inundated, including loss of life of 50 people (Larson, 1997).

The "Great USA Flood of 1993" is not an isolated event. Such widespread precipitation induced extreme events continue to occur in the United States. For instance, according to the billion-dollar weather and climate disasters catalog released by the NOAA/National Centers for Environmental Information (NCEI) for the Year 2018, there were 12 storms that occurred across the United States including eight severe storms, two tropical cyclones named Hurricane Florence and Hurricane Michael, respectively, and two winter storms. Together, they caused $64 billion (U.S. dollars) economic damages, and they amount to 70% of total losses associated with all of the billion-dollar disasters that occurred throughout the United States in 2018 (NOAA/NCEI, 2019). Identifying the ground footprint of extreme precipitation events and modeling their spatial risk using large-scale atmospheric processes would be of immense value for determining the probability of a specific region -where and when- undergoing a high risk of inundation and sudden deluge. It has invaluable beneficial effects in terms of better management of the infrastructure systems and reducing the risk to the society.

1.2. Related Studies

We now briefly underline the recent advances that are in close connection to understanding the spatial extent of precipitation extremes. Excepting the work of Touma et al. (2018), that quantified the length scales of extreme precipitation events (>90th percentile) within a 500 km radial neighborhood across the United States during 1965–2014, and Kunkel and Champion (2019) that studied the top 100 largest area-averaged precipitation events in the United States during 1949–2018, current understanding of the spatial manifestation of extreme precipitation events at the land surface level is limited to regional exploratory analyses, specific seasons/events, or using restricted records of data (e.g., Mason et al., 1999; Zhang et al., 2001; Voskresenskaya & Vyshkvarkova, 2016, and recent works by Berghuijs et al., 2019, & Kunkel et al., 2020, respectively, on trend detection of synchronous flooding and average return intervals of extreme precipitations). AghaKouchak et al. (2011) compared the connectivity of rainfall fields derived from satellite data with a reference radar pattern for multiple satellite images during Hurricane Rita near the U.S. Gulf Coast that occurred in September 2005. Zepeda-Arce et al. (2000) studied the structure of the observed storms in Oklahoma and developed a predictive scheme based on convective available potential energy. A more detailed description of their work can be found in Foufoula-Georgiou and Vuruputur (2001), where they ask an important question on whether rainfall spatiotemporal patterns exhibit organization and if so, would they be related to the physics of the atmosphere. An automated rainfall classification framework using a combination of gamma distribution and cluster analysis was developed by Baldwin et al. (2005) (Baldwin Object-Oriented Identification Algorithm or BOOIA) to model morphological properties of 148 rainfall events in the United States using an hourly precipitation data set. Later, Hitchens et al. (2012) used the BOOIA for the characterization of extreme precipitation and identifying their causative mesoscale convective systems (MCSs) over the Midwestern United States between 1996 and 2010. Similarly, Chang et al. (2016) proposed a statistical simulation algorithm to assess possible changes that might be seen in intensity, size, and duration of future precipitation patterns, conditional on warmer temperatures across the United States. Further studies that examine MCS for thunderstorms can be seen in works performed by Johns (1993), Bentley and Mote (1998), Trapp et al. (2005), and Lu et al. (2015). The duration and spatial extent of global extreme precipitation was investigated by Dwyer and O'Gorman (2017) using global climate

model simulations over the midlatitudes. They noticed a decreased duration over the 21st century projection. Recently, the areal extent of extreme rainfall was empirically identified to follow power laws, hence explaining the underlying self-organization and scaling behavior (Devineni et al., 2015).

In Europe, the homogeneous patterns of precipitation were analyzed by Tabony (1981) where they indicated that there is a gradient in rainfall from north to south and over the United Kingdom, Wales, and Ireland together with common phase and amplitude in the southwestern and central England and over Wales. They also highlighted that a combination of regional factors and large-scale atmospheric processes would define such precipitation patterns at different spatial scales. Similarly, in the Himalayan region, Anders et al. (2006) explained that there is a notable east-west tending and ridge-valley spatial gradient of precipitation patterns, which are strongly governed by the topographical differences. Kansakar et al. (2004) conducted a detailed study of spatial properties for different precipitation regimes across Nepal. They elaborated on the role of high-mountainous areas in causing the orographic lifting and influencing the rate of precipitation in the windward/leeward sides. In Australia, Wasko et al. (2016) showed that storm patterns will be less uniform at higher temperatures, according to the scaling of the extreme rainfall with warmer temperature at or above the Clausius-Clapeyron rate. A few other related regional studies can be found in Esteban-Parra et al. (1998), Cavazos (1999), Peñarrocha et al. (2002).

There is a large body of literature which examines the relationship between large-scale atmospheric circulations and regional precipitation patterns (e.g., Liu et al., 2020, and references therein). Wang and Chen (2009) showed that the Great Plains low-level jet (GPLLJ) can be attributed to late-spring extreme rainfall events over the central United States. The incoming northward tropical moist air masses from the Gulf of Mexico can further enhance the occurrence of such extreme rainfall events with devastating floods in the late spring and the summer seasons (Hitchens et al., 2012; Lu & Hao, 2017; Najibi et al., 2019). In summer, the frequency and distributions of rainstorms are associated with the midtropospheric perturbations caused mostly by the northwest flow severe weather outbreaks (Johns, 1982; Wang et al., 2011). Smith et al. (2013) demonstrated that the frequency of severe thunderstorm gust features a primary corridor over the Southern and Central Plains, while around 50% of the wind gusts between 2003 and 2009 are distributed from immediate leeward side of the Rockies into the Intermountain West of the United States. Smith et al. (2012) provided a large database of thunderstorms for the United States (2003–2011) and discussed the possible causes of different spatial patterns; for example, the right-moving supercell events mostly occurring in May and September are caused by the tropical cyclones. Recently, Kunkel et al. (2019) and Mondal et al. (2020) studied the relationships between precipitable water and annual precipitation maxima, and the properties of summer extreme precipitation events, respectively. Also, Jiang et al. (2020) used daily precipitation during August–October (1,140 stations and 6,164 days) to explore the generic distribution of dominant precipitation modes and their relationships with El Niño–Southern Oscillation (ENSO). A majority of these studies are limited to regional/seasonal scales and/or an event-based investigation of the spatial fields with explanatory analysis of their attributable climate and atmospheric circulation features.

This extensive survey has shown us that there is a high demand for a systematic study to quantify the spatial manifestation of simultaneous extreme precipitation across the conterminous United States, determine their area scaling factors and atmospheric patterns, and statistically model them for future predictions and portfolio risk management strategies. Hence, in this paper, we introduce simultaneous heavy precipitation event (SHPE) as a new form of measuring the spatial structure of heavy precipitation events. We also investigate the potential causes and drivers that led to such spatial organization throughout the United States. Furthermore, we present the quantification of the areal extents of SHPEs using power laws and a relatively simple logistic modeling scheme to predict the risk of SHPEs spatially over the United States.

The rest of the paper is structured as follows: Section 2 describes the data and observations that were employed in this analysis. The methodology and the geometric indicators are presented in section 3. In section 4, we explain the spatial characteristics of SHPEs in the 20th and early 21st centuries (1900–2014) across the United States together with their areal extent scaling relationships, seasonality, associated atmospheric dynamics and climatic processes, and predictive model. Final conclusions and remarks are presented in section 5.

2. Materials and Data Preparation

2.1. Precipitation: GHCN-Daily Observations

Long-term records of daily ground-based precipitation measurements over the contiguous United States between 1900 and 2014 (115 years) are obtained from the Global Historical Climatology Network-Daily (GHCN-D) (Menne et al., 2012; NOAA/NCDC, 2017). The GHCN-D data can be accessed from the NOAA's National Centers for Environmental Information (NCEI). We selected 1,244 stations with nearly full records across the conterminous United States using a two-stage filtering process. In the first stage, for all the available stations, we flagged any year with more than 72 days of missing data (20%) as "missing years." Then, we selected those stations that have at least 92 years of complete data (i.e., less than 20% missing years). We used this 1,244-station data in a recent study on identifying trends in the frequency of extreme rainfall days (Armal et al., 2018). There are 42,003 days in the analyzed data set.

The main reason for using ground-based precipitation observations is to overcome the shortcomings attributed to gridded precipitation products at the national scale, especially for extreme precipitation analysis. For instance, several of the gridded products appear to underestimate extreme precipitation (e.g., Risser et al. (2019),Timmermans et al. (2019), Daly et al. (2017) and references therein). This underestimation is even more prominent at higher altitudes and while capturing local extremes (e.g., Gervais et al., 2014). We intended to avoid such systematic data-related issues. Moreover, gridded precipitation products are also substantially shorter in record length compared to ground-based observations.

2.2. Atmospheric Circulation Based on Reanalysis

We used the European Centre for Medium-Range Weather Forecasts (ECMWF) 20th Century Reanalysis (ERA-20C; Hersbach et al., 2015) from 1900 to 1978 and the ERA-Interim (Dee et al., 2011) from 1979 to 2014. For both reanalyses, we downloaded data that ECMWF had projected onto a 1.5° horizontal resolution. The twentieth century reanalysis is available through 2014. However, ERA-Interim uses a more comprehensive data assimilation procedure. ERA-20C and ERA-Interim are compiled into a continuous data set, and it is utilized to create composites for 500-hPa geopotential heights (Z_{500}) and precipitable water vapor (PWV). A 115-year daily climatology based on 1900 to 2014 is created for geopotential heights, and used for calculating the anomaly field of each variable.

3. Methods and Setup

In Figure 1, we present the workflow diagram for the systematic approach that was carried out in this study. We introduced the first module, which is related to the preparation of data, in section 2 (Materials and Data Preparation section). The remaining sections that are about the spatial representation of precipitation extremes will now be explained in detail.

3.1. Defining SHPEs

We start by presenting two examples of the spatial manifestation of widespread rainfall that occurred on 8 May 1995, and 13 September 1961 (Figure 2a). The algorithm described below shows how to identify SHPEs. An illustration is provided in Figure 2b to contextualize each step.

1. The 99th percentile (hereafter, R_{99}) of the daily nonzero precipitation intensity (R, millimeters) —across all 115 years of daily records— is computed for each of the 1,244 GHCN-D stations.
2. For each day starting from 1 January 1900 to 31 December 2014, we count the number of rainfall stations that have a measured precipitation intensity greater than 0 (i.e., $R > 0$) and label them as c_1 (light-blue colored stations in Figure 2b). Next, we examine if any stations listed in c_1 have a precipitation intensity greater than R_{99} (i.e., $R > R_{99}$), and define them as c_2 (dark-blue colored stations in Figure 2b). c_2 is the total number of stations (if any) that recorded an extreme precipitation intensity (>99th percentile) on that day.
3. Then, we calculate the rate of extremes (RoE) as $RoE = c_2/c_1$. RoE for a day indicates what fraction of the rain gages recording nonzero precipitation are experiencing an extreme rainfall intensity ($R > R_{99}$). We then calculate the 99th percentile of the distribution of RoE, RoE_{99} (Figure 2c). RoE_{99} indicates a threshold RoE where a substantial number of rain gages simultaneously observed extreme precipitation. In our case, $RoE_{99} = 0.15$; 15% of the rain gages that measured nonzero rainfall are simultaneously experiencing extreme rainfall. This threshold helps us identify only those notable stations that are experiencing simultaneous heavy precipitation for any specific day.
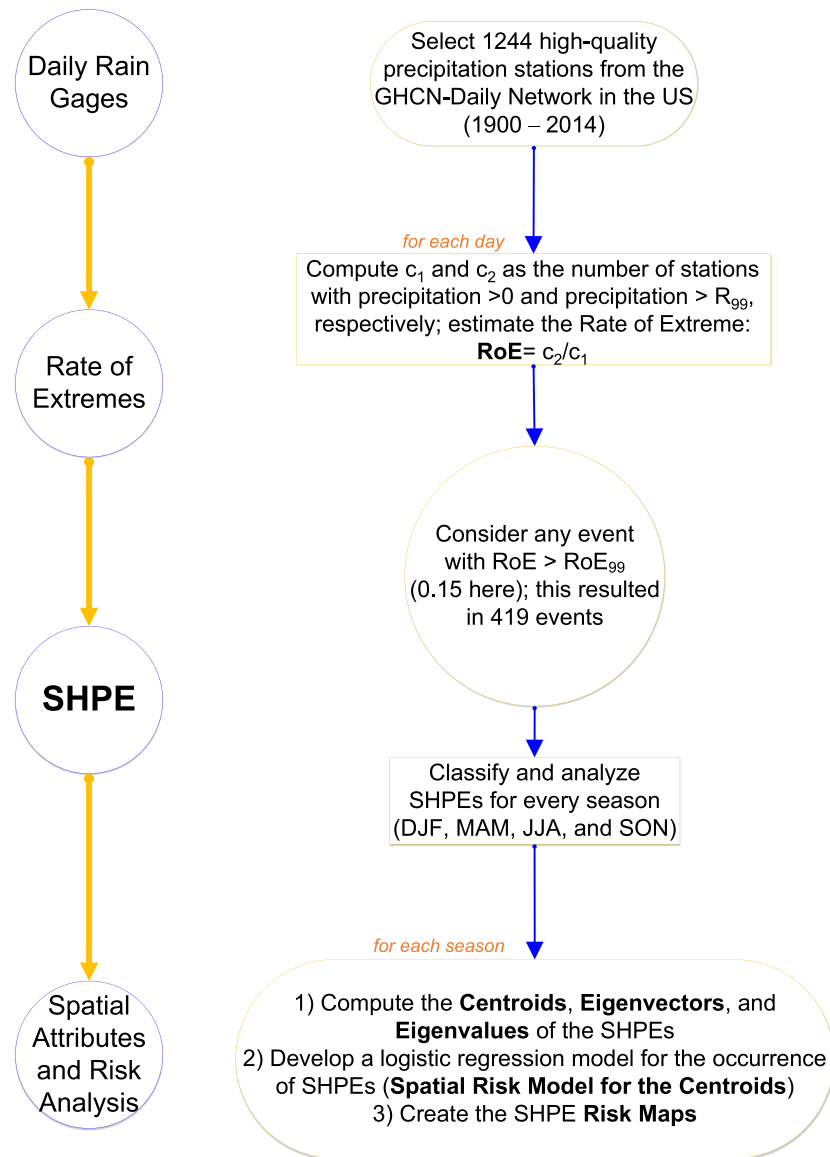
Figure 1. Workflow diagram presenting the approach for understanding and modeling the spatial characteristics of simultaneous heavy precipitation events (SHPEs) across the conterminous United States.

4. Ultimately, we admit those days (i.e., events containing a certain number of stations) that satisfy the condition $RoE > RoE_{99}$ into the SHPEs database for the 1900–2014 period. *An SHPE indicates a spatial structure of intense precipitation on the land that has been recorded by a significant number of stations on a given day*. To account for the uncertainty in identifying SHPEs due to the space-time disparity in the measurement of precipitation with the movement of the storm, we also include any stations with extreme precipitation intensities 1 day before and 1 day after the SHPE date. For example, an event that lasted for 4 h from 10 p.m. of the current day to 2 a.m. of the next day can be recorded in both the days if it is over one station, or can be recorded in multiple stations over the 2 days. We consider this phenomenon as one event. In other words, we perform a 3-day smoothing for each SHPE to adjust our database to account for extremes of the previous day and the next day. Note that we are using daily precipitation and not individual storms. In this regard, an intense storm happening over a short duration, if occurred during the daily transition (e.g., between 10 p.m. and 2 a.m.), may not show up in SHPEs due to aggregation by the days.
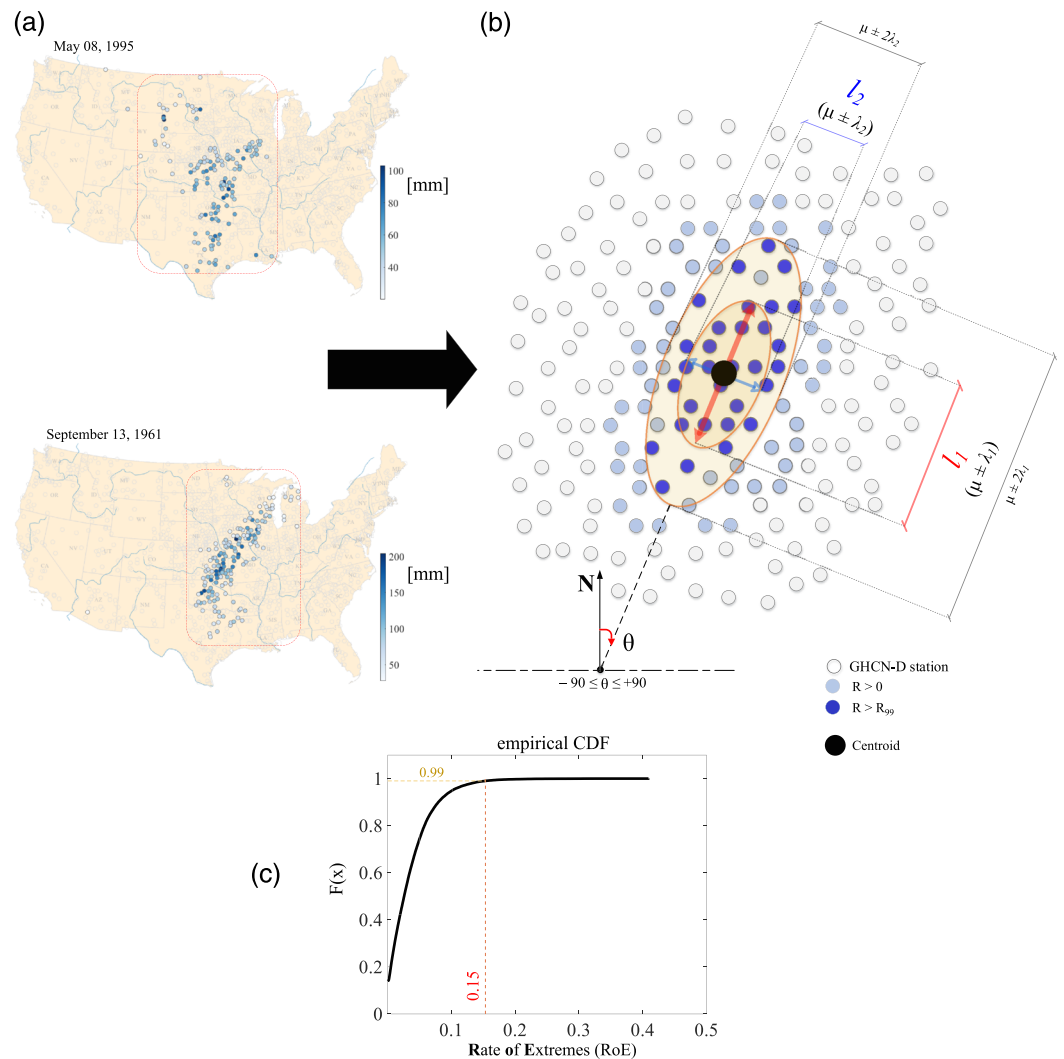
Figure 2. (a) Spatial distribution of two widespread precipitation events that occurred on 8 May 1995 (top) and 13 September 1961 (bottom), and (b) geometric illustration of the extent of an SHPE on the ground. The stretches are shown as l_1 and l_2 axes, and the orientation angle is shown as θ. Note that depending on the manifestation of the SHPE on the ground, θ > 0 indicates SW-NE direction (as shown in the illustration) and θ < 0 indicates SE-NW direction. The dark filled circle (μ[*lon, lat*]) indicates the centroid, and λ_1 and λ_2 refer to the eigenvalues of the SHPE. (c) The empirical cumulative distribution function (CDF) of the rate of extremes (RoE) is indicated. The 99th percentile of events that have $RoE > RoE_{99}$ (i.e., $RoE_{99} = 0.15$) are selected in this study. The two SHPEs shown here in panel (a) contain 207 and 271 stations, respectively, with l_1, l_2, θ of 1,250 km, 903 km, -50.42° and 1,162 km, 738 km, 46.29°. Their centroids are located at 97°W, 39°N (near Junction City in Geary county, KS) and 94°W, 38°N (Ballard in Bates county, MO), approximately. The SHPE in May 1995 attributes to May 1995 Louisiana flood, impacting the states of Kansas, Missouri, Nebraska, Oklahoma, Mississippi, and Louisiana with total losses tallying $3 billion (U.S. dollars). The SHPE in September 1961 is related to Hurricane Carla (1961) causing more than $300 million damage to the states in the central United States.

By applying the above described detection algorithm, we identified 419 SHPEs over the conterminous United States between 1 January 1900 and 31 December 2014. Since there is a clear seasonality in precipitation across the United States, we classify the 419 SHPEs into four formal seasons listed as December-January-February (DJF), March-April-May (MAM), June-July-August (JJA), and September-October-November (SON). This classification will also help explore the spatial characteristics of SHPEs and their synoptic circulation patterns. There are 54, 58, 103, and 204 SHPEs, respectively, in DJF, MAM, JJA, and SON seasons.

3.2. Centroids, Principal Axes, Areal Extents, and Orientations of SHPEs

We quantify SHPEs using their geometric properties; centroids, the two principal axes of spatial variance along with their orientation, and the areal extents. In Figure 2b, we show a black filled circle as the centroid of the SHPE, and two vectors, l_1 and l_2 as the first (major) and second (minor) axes of a typical SHPE with elliptical manifestation. In addition, we also determined the orientation of the principal axis; the angle between the major axis (l_1) and the Earth's geographic north (N, 0° azimuth angle). The orientation angle is referred to as θ hereafter (see Figure 2b).

Each SHPE is made up of a vector of coordinates (the longitude and latitude, [lon, lat]), that essentially constitute the spatial manifestation of extreme rainfall. After excluding the outliers, the centroid for a finite set of the coordinate vector space is computed using the discrete approximation of the joint first moment.

For each season,

$$\mathbf{Centroid}_{shpe}^{j} = \left(\frac{1}{n} \sum_{i=1}^{n} lon_i^j, \frac{1}{n} \sum_{i=1}^{n} lat_i^j \right) \tag{1}$$

where j indicates the number of identified SHPEs in that season (e.g., $j = 1$ to 54 for DJF) and n is the total number of stations for that SHPE. **Centroid** is the centroid matrix with a size of two ([lon, lat]) by the total number of SHPEs in each season.

While our choice of a high RoE threshold (RoE_{99}) ensured that the SHPEs were spatially homogeneous, we found a few events having disparate manifestation with pockets of outlying stations predominantly in the longitudinal direction. This pattern is expected since, on any given day, one could find stations that are far apart, recording extreme rainfall simultaneously. For example, one could find a situation where an Atlantic hurricane causes an SHPE, while at the same time, stations far away from this hurricane track could experience extremes due to deep convection. Hence, we opted to identify and exclude these outlier stations.

The procedure for identifying the outliers for SHPEs is described below:

1. We first compute the median ($\widetilde{lon}$) and the interquartile range (IQR) of the longitudes for each of the SHPE in a given season. While median indicates a robust central location in the longitudinal direction, IQR (computed as the difference between the 75th and 25th percentiles of the distribution of longitudes), provides a robust distance measure for the SHPE range over the longitudinal direction.
2. We then compute the absolute deviation of each station from $\widetilde{lon}$ ($AD_i = |lon_i - \widetilde{lon}|$) to measure the longitudinal distance for each station from its longitudinal center. Large (small) AD_i indicates a station that is far away from (close to) the central location. We compare AD_i (distance) for each station with a cutoff distance, which is the 95th percentile of the IQRs across all events in the season. Any station with $AD_i > IQR_{95}$ is considered as an outlier and excluded from the coordinate vector. As mentioned before, we had very few events that needed this filtering, but the process was essential to ensure that the **Centroid**$_{shpe}$ is resistant to outliers.

To get the major and minor principal axes, and the orientation of the SHPE (indicated as l_1, l_2, and θ in Figure 2b), we applied principal component analysis (PCA) (i.e., empirical orthogonal function analysis) (Wold et al., 1987) on the coordinate vector space. We implemented PCA in two dimensions to derive the two eigenvalues (λ_1 and λ_2) and the eigenvectors (E). PCA will map the SHPEs coordinate vector space onto a new rotated space so that the major principal axis (l_1) will be in the direction of the maximum variance while the minor principal axis (l_2) will be perpendicular to this axis. The two eigenvectors, which determine the magnitude of the rotation, are used to derive the orientation angle (θ). Essentially, we decompose the covariance matrix of the coordinate vector space into an orthogonal matrix of eigenvectors and a diagonal matrix with eigenvalues as its nonzero diagonal elements.

$$\begin{bmatrix} \sigma_{lon}^2 & \sigma_{lon}\sigma_{lat} \\ \sigma_{lon}\sigma_{lat} & \sigma_{lat}^2 \end{bmatrix} = [E] \begin{bmatrix} \lambda_1 & 0 \\ 0 & \lambda_2 \end{bmatrix} [E]^T \tag{2}$$

We assume l_1 as $\mu \pm \lambda_1$ and l_2 as $\mu \pm \lambda_2$ to get the lengths of the axes in both directions from the centroid. Each SHPE is hence transformed into an ellipse with a centroid (Centroid$_{shpe}$ = $[lon, lat]$) and two axes of l_1 and l_2.

The ratio of l_2/l_1 is also computed for each SHPE to see if the geometric structure is circular or elliptical. Larger l_2/l_1 ratios would refer to circular SHPEs, whereas, if $l_1 \gg l_2$, the areal extent of SHPEs will be placed mostly along the l_1 axis and the structure of the SHPE will be elliptical. The areal extent for each SHPE is also calculated based on $area = \pi l_1 l_2$, where $l_1 = 2\lambda_1$ and $l_2 = 2\lambda_2$ as shown in Figure 2b. We are assuming that $l_1 = \mu \pm \lambda_1$ and $l_2 = \mu \pm \lambda_2$ here, that is, the high density part that covers approximately 66% of the mass. One can also compute the area for the full SHPE ellipse where l_1 and l_2 can be assumed as $\mu \pm 2\lambda_1$ and $\mu \pm 2\lambda_2$.

Furthermore, we computed SHPE's orientation, which indicates its angle with respect to the geographical north direction (azimuth). This angle identifies the angular distance between SHPE's major axis (i.e., l_1) and N (N is the 0° azimuth degree for the Earth's geographic North Pole) (see parameter θ in Figure 2b). The angle θ is calculated using eigenvectors, which range from -90° to +90° (where 0° is set toward the Earth N direction; 0° azimuth) for the negative (SE-NW) and positive (SW-NE) orientations of SHPEs, respectively.

4. Results and Discussions

4.1. Temporal Characteristics of SHPEs Across the United States (1900–2014)

Based on the detection algorithm described in section 3, we identified 419 SHPEs out of the 42,003 days between 1 January 1900 and 31 December 2014 (approximately 1% of the days). Figure 3 presents the temporal distribution of these 419 SHPEs across the United States at the daily, seasonal, and annual time scales.

For each event, we recorded the day of year (DOY), a sequence number indicating 1 if the SHPE occurred on 1 January, and 365 or 366 if the SHPE occurred on 31 December (a leap year with 366 days). Figure 3a shows this intra-annual distribution as a scatterplot in the polar coordinate system. SHPEs are occurring throughout the year with a slightly increased frequency in the second half of the year. SHPEs in February and March have the lowest frequency (in total, 10 and 7 SHPEs occurred in February and March during 1900–2014).

We also computed the number of SHPEs occurring each year (1 January to 31 December) and each season of the year (DJF, MAM, JJA, and SON) over the entire time period (1900–2014). The annual frequency time series plot along with a LOWESS (Locally Weighted Scatterplot Smoothing Loader, 2006) line is shown in Figure 3b. While the mean annual sum of SHPEs is between 3 and 4, we observed a convex behavior with more SHPEs in the early 20th and early 21st centuries. There were 196, 150, and 73 SHPEs that occurred in the periods of 1900–1950, 1951–2000, and 2001–2014, respectively, in the United States. A simple Mann-Kendall nonparametric trend test (Mann, 1945) on the annual frequency reveals no significant trend (p value = 0.75).

The time series of the seasonal counts are shown in the inset of Figure 3b. It has to be noted that the seasonal counts of DJF include SHPEs from December of the previous year. For example, DJF for the Year 2000 contains SHPEs that occurred in December 1999 and in January and February of 2000. As in the case of the annual frequency, we failed to detect any seasonal trends over the years. The SHPEs during the SON season have a higher frequency in particular when compared to the other three seasons.

4.2. Spatial Characteristics of SHPEs Across the United States (1900–2014)

4.2.1. SHPEs in December, January, and February

Figure 4 presents the spatial distribution of the geometric attributes of SHPEs that occurred during the DJF season (i.e., any SHPEs dated in December, January, or February; DOY between 335 and 59 or 336 and 60 for leap years) from 1900 to 2014 across the conterminous United States. The centroid and two axes for each SHPE (i.e., major and minor axes of the ellipse) are sketched as a filled black circle and red thick and blue thin lines (l_1 and l_2), respectively.

There are 54 SHPEs in the DJF season of which 37 (~70%) occurred over the Cascade Range and the U.S. Pacific coast region, that is, mostly in the states of Washington, Oregon, Nevada, and over Northern California. The average length of the l_1 and l_2 axes are approximately 1,100 and 550 km. SHPEs with short l_1 can be seen across the U.S. Pacific coast region. The ratio of l_2 to l_1 is mostly greater than 0.5 for SHPEs in the Pacific Northwest, indicating a more circular spatial manifestation (see Figure 4b). However, the 17 SHPEs that did not occur in the Pacific coast region —but occurred over Ohio Valley and west north central— have more areal aggregation along the l_1 axis, and thus the ratio of l_2 to l_1 is lower than 0.5. The spatial manifestation of these 17 SHPEs is mostly elliptical. Additionally, Figure 4c shows the calculated area
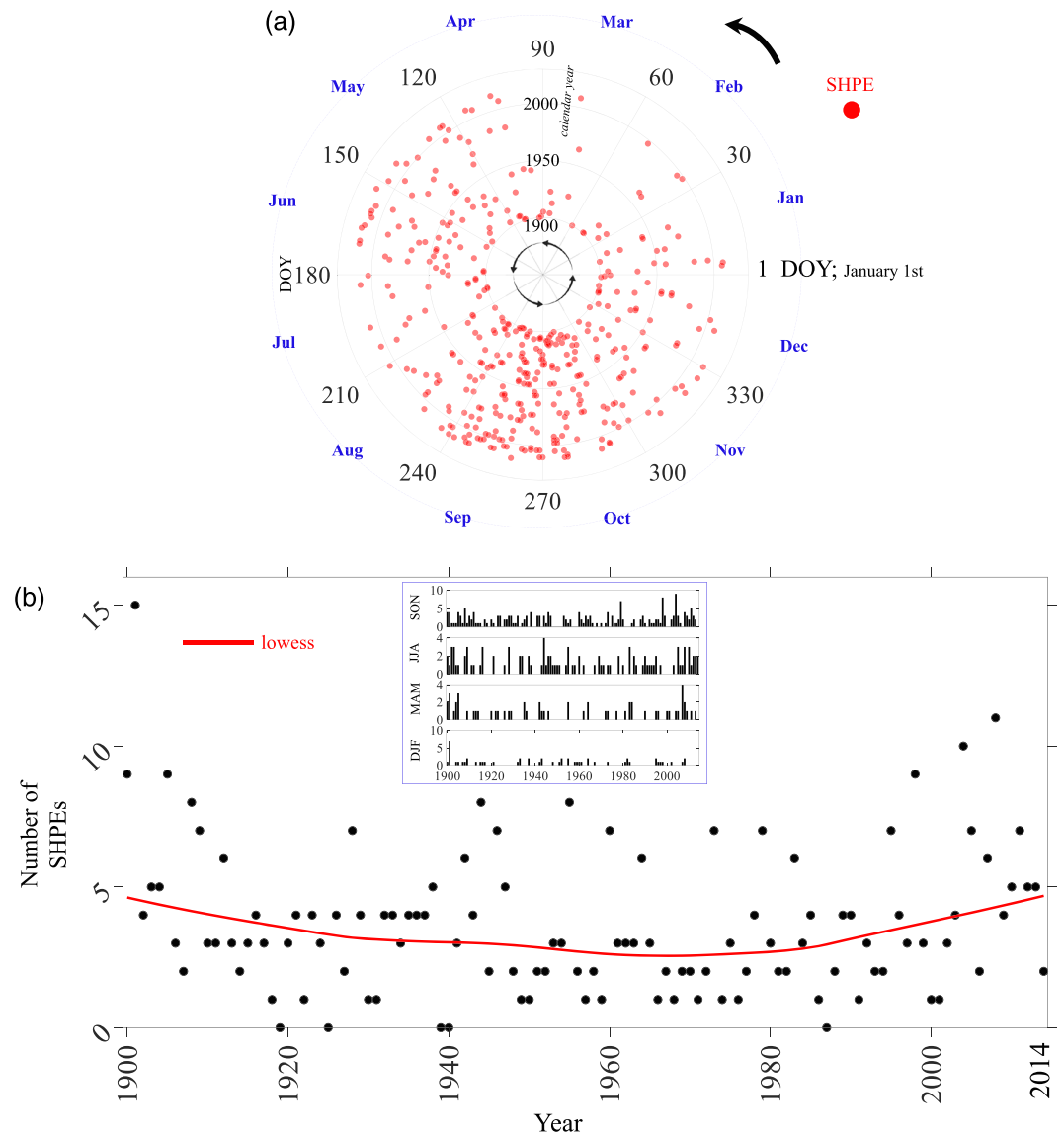
Figure 3. (a) Time of occurrence of SHPEs within the years between 1 January 1900 and 31 December 2014 is presented as a scatterplot in the polar coordinate system. The date 1 January is set as DOY (day of year) equal to 1, and the annual cycle ends on 31 December in each year. (b) Temporal distribution of the annual counts of SHPEs (419 events between 1900 and 2014) with the LOWESS smoother plot. The seasonal counts of SHPEs for four seasons, December-January-February (DJF), March-April-May (MAM), June-July-August (JJA), and September-October-November (SON) is shown in the inset of this panel.

for each SHPE (approximated as the area of the ellipse) in units of square kilometers. The corresponding areas cover an extent equal to 2,100,000 km^2 on average where larger areas are dominant for those SHPEs manifested across the states of Missouri, Oregon, Nevada, and over Northern California. Also, most of the SHPEs in the DJF season have a SW-NE orientation as the l_1 axis points to the SW-NE direction toward the North Pole (i.e., positive θ angles).

4.2.2. SHPEs in March, April, and May

We identified 58 SHPEs in the MAM season during 1900–2014 across the conterminous United States. The spatial manifestation of these SHPEs including their two axes (l_1 and l_2) with orientation and circular or elliptical manifestation (ratio of l_2 to l_1), as well as their full quasi-elliptical areas are shown in Figure 5.

Figure 5a shows that the central and south central United States is the footprint for most SHPEs that occurred during the MAM season. In particular, the states of Kansas, Oklahoma, and Nebraska have more SHPEs
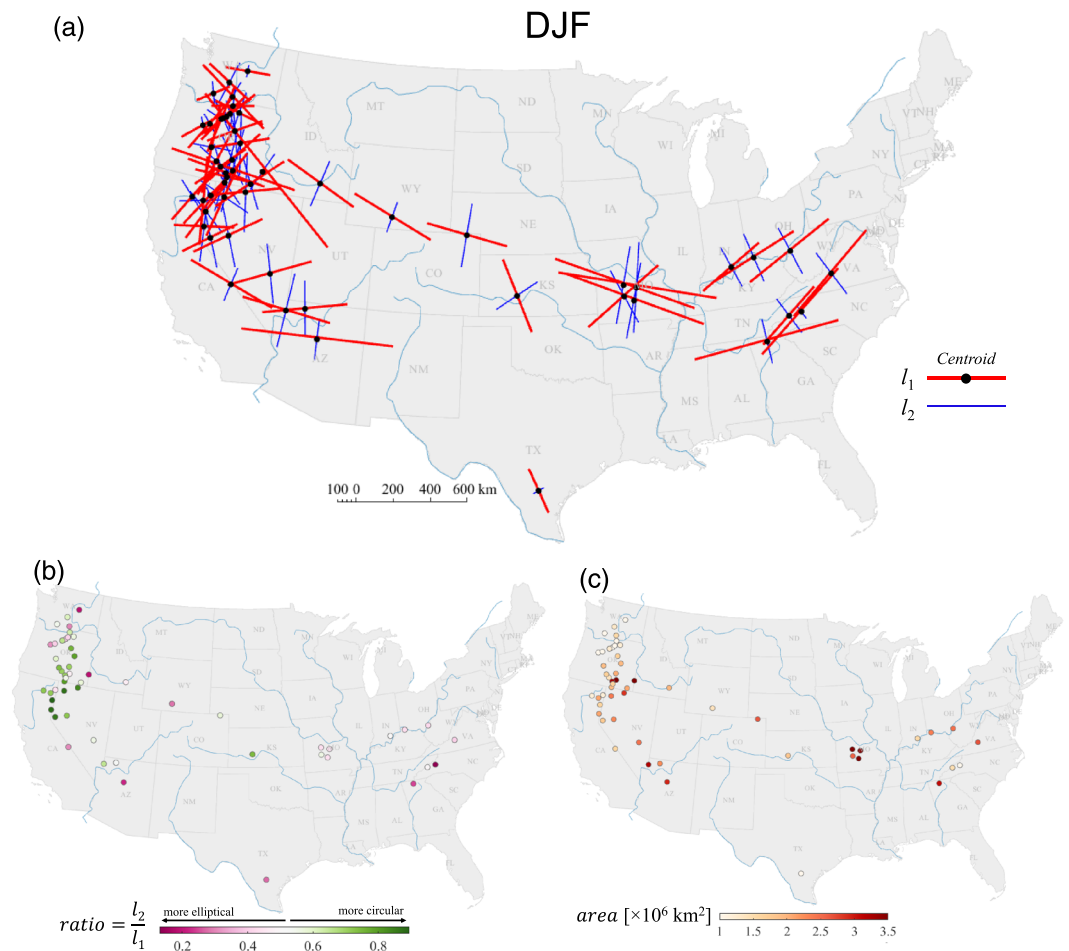
Figure 4. (a) Spatial distribution of SHPEs in the DJF season shown using their centroids and stretches (l_1 and l_2 axes) (1900–2014), (b) distribution of l_2/l_1 ratio to indicate the elliptical and circular nature of SHPEs, and (c) areal extents of SHPEs (readers are cautioned against the projection artifact that might be influencing the orthogonality of l_1 and l_2 axes).

with a circular structure and have larger areas (2,000,000 to 2,500,000 km²). The States of Missouri, Iowa, and Illinois have SHPEs with mostly elliptical structures with smaller areas compared to the circular SHPEs (see Figure 5b). There are 8 SHPEs (out of the 58) that occurred along the U.S. northeast belt that mostly have smaller areas and SW-NE azimuth orientation.

60% (40%) of the 58 SHPEs have a SE-NW (SW-NE) orientation. The circular SHPEs (dominant in the central United States) mostly have a SE-NW orientation (negative θ) while the elliptical SHPEs (dominant in the eastern United States) have a SW-NE orientation (positive θ) during the MAM season. There is evidence that most of the SHPEs in this season were responsible for major floodings in the central and south central United States in the late spring and early summer. For example, a continuous 40-hr heavy rain episode led to the "May 1995 Louisiana Flood" (Ricks et al., 1997; Vatti et al., 2003). We illustrated its possible SHPE in Figure 2a (top) that occurred on 8 May 1995 over the central United States. This SHPE features a SE-NW direction ($\theta = -50.42°$) and l_1, l_2, and areal footprint equal to 1250, 903 km and 3,500,000 km². It caused a devastating flood across multiple rivers in the states of Kansas, Arkansas, Illinois, Missouri, Mississippi, and Louisiana in May and early June 1995, in addition to $3.1 billion (U.S. dollars) in damage. The Missouri and Mississippi Rivers crested at 11.19 and 14.23 m, which was 3.57 and 4.48 m above the flood stage, respectively (Turnipseed et al., 1995).

4.2.3. SHPEs in June, July, and August

For the June, July, and August (JJA) season, we detected 103 SHPEs from 1900–2014. Most SHPEs in the JJA season are spread over the U.S. Midwest and over the East Coast and northeast regions (Figure 6). South
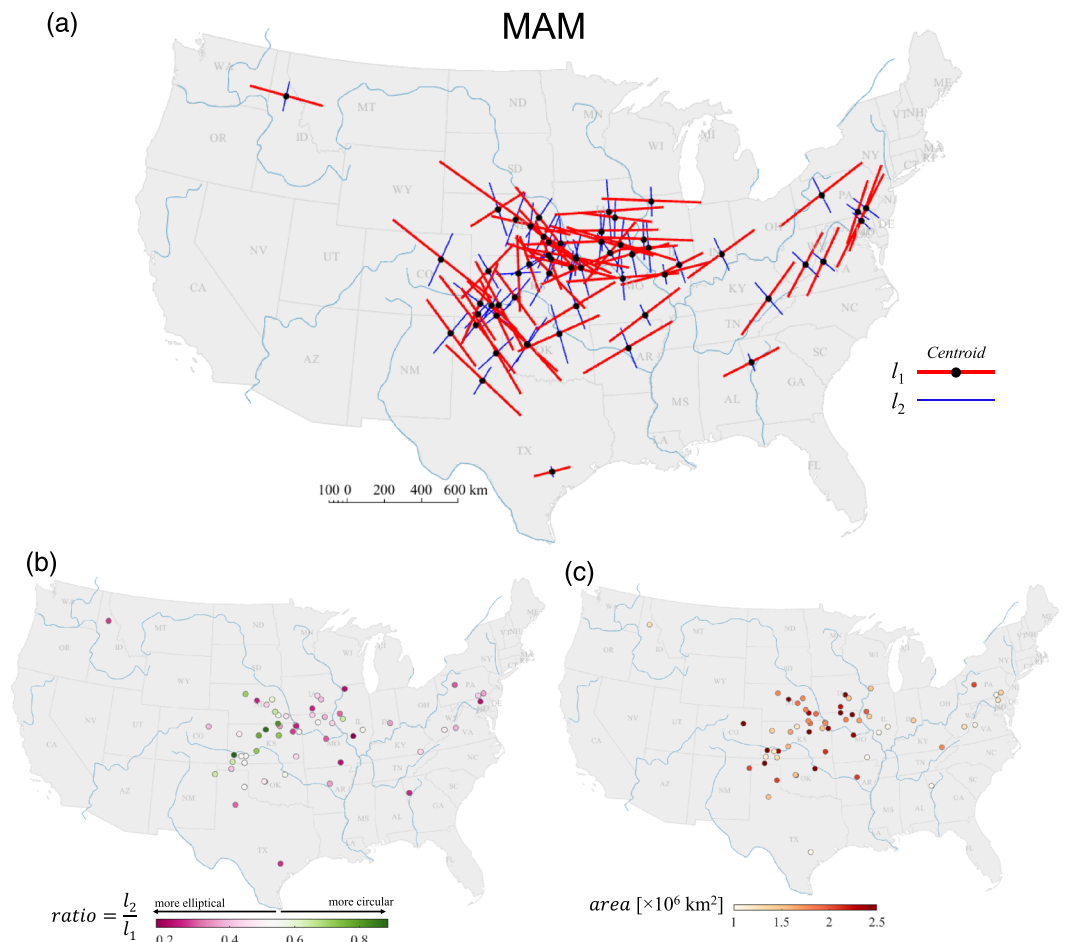
Figure 5. (a) Spatial distribution of SHPEs in the MAM season shown using their centroids and stretches (l_1 and l_2 axes) (1900–2014), (b) distribution of l_2/l_1 ratio to indicate the elliptical and circular nature of SHPEs, and (c) areal extents of SHPEs (readers are cautioned against the projection artifact that might be influencing the orthogonality of l_1 and l_2 axes).

Dakota, Nebraska, Iowa, Missouri, Kansas, Kentucky, and Illinois are the primary States in the Midwest that were impacted by these SHPEs. While the majority of SHPEs that occurred over the Midwest and northeast indicate an elliptical spatial structure, those SHPEs that occurred across the states of Nebraska and Kansas are mostly circular in shape (see Figure 6b).

SHPEs in this season have areal extents averaging around 2,300,000 km^2. In particular, Midwest-related SHPEs have an area that mostly ranges from 2,500,000 to 4,400,000 km^2 (see Figure 6c). Moreover, the orientation of SHPEs in the JJA season is aligned toward the SE-NW direction (negative θ). See, for instance, the events in the Midwest over the Missouri River Basin (and leeward of the Rocky Mountains).

Referring back to the "Great USA Flood of 1993", our results showed that an SHPE containing over 120 rainfall gauges occurred on 8 June 1993. This elliptical SE-NW SHPE (ratio = 0.36, $\theta = -80°$) manifested over the state of Iowa (centered at 42.5°N and 92.0°W) with an average intensity of 50 mm (maximum of 136 mm), and l_1 and l_2 of 1,600 and 580 km, respectively.

We also noticed two similarly strong SHPEs that occurred back-to-back on 30 and 31 August 2005, with an average rain intensity of 80 mm (maximum of 230 mm) from over 130 rain gauges. They were centered over the state of Kentucky along the SW-NE direction with areal extents almost equal to 3,000,000 km^2, crossing the states of Mississippi, Tennessee, Kentucky, Indiana and Ohio. One can associate these two SHPEs as the full footprint of Hurricane Katrina (2005) after the landfall, a Category 5 hurricane that occurred in late August 2005, causing $125 billion (U.S. dollars) in damage.
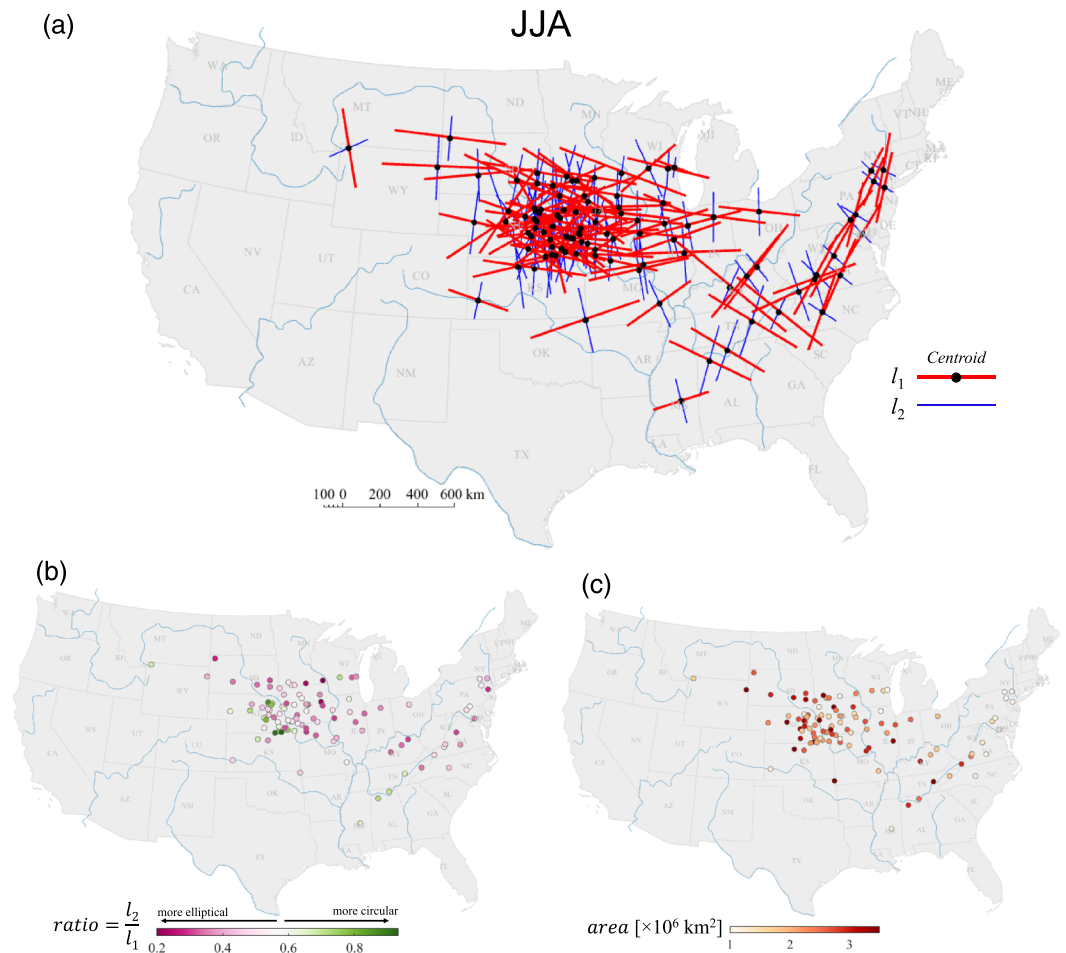
Figure 6. (a) Spatial distribution of SHPEs in the JJA season shown using their centroids and stretches (l_1 and l_2 axes) (1900–2014), (b) distribution of l_2/l_1 ratio to indicate the elliptical and circular nature of SHPEs, and (c) areal extents of SHPEs (readers are cautioned against the projection artifact that might be influencing the orthogonality of l_1 and l_2 axes).

4.2.4. SHPEs in September, October, and November

There are 204 SHPEs in this season during 1900–2014 across the conterminous United States. We recognize three spatial clusters that manifested regionally over the United States, including the U.S. West Coast, the Midwest, and the northeast/Mid-Atlantic regions (Figure 7). There is a high incidence of SHPEs across the northeast/Mid-Atlantic region in particular over the states of New York, Pennsylvania, Maryland, Virginia, West Virginia, North Carolina, South Carolina, as well as the States of Georgia and Kentucky. In addition, the States of Iowa, Nebraska, Missouri, Kansas, and Illinois are mostly the target regions of Midwest-related SHPEs (Figure 7a). There are a few SHPEs that manifested over the states of Oregon and Washington (the cluster in the West Coast). Although the orientation of SHPEs in the SON season mostly follow a SW-NE direction (positive θ), we can see a mixture of SW-NE and SE-NW directions for SHPEs in the U.S. Midwest.

As before, we calculated the ratio of l_2 to l_1 for SHPEs in the SON season and presented them in Figure 7b. It is apparent that the majority of the SHPEs that occurred across the Midwest region have mostly circular structures, while SHPEs in the northeast/Mid-Atlantic region indicate elliptical spatial structures. Their calculated areas are presented in Figure 7c. The average area for SHPEs in this season is approximately 1,900,000 km². Most of the SHPEs with larger areal extents were manifested in the Midwest region. Hurricane Carla (1961) (see Figure 2a, bottom) and Hurricane Ike (2008) (which can be linked to two consecutive SHPEs on 13 and 14 September 2008) are just a few examples of hurricane induced SHPEs in this region. SHPEs in the U.S. West Coast spatial cluster have significantly smaller areal extents with a SW-NE orientation.
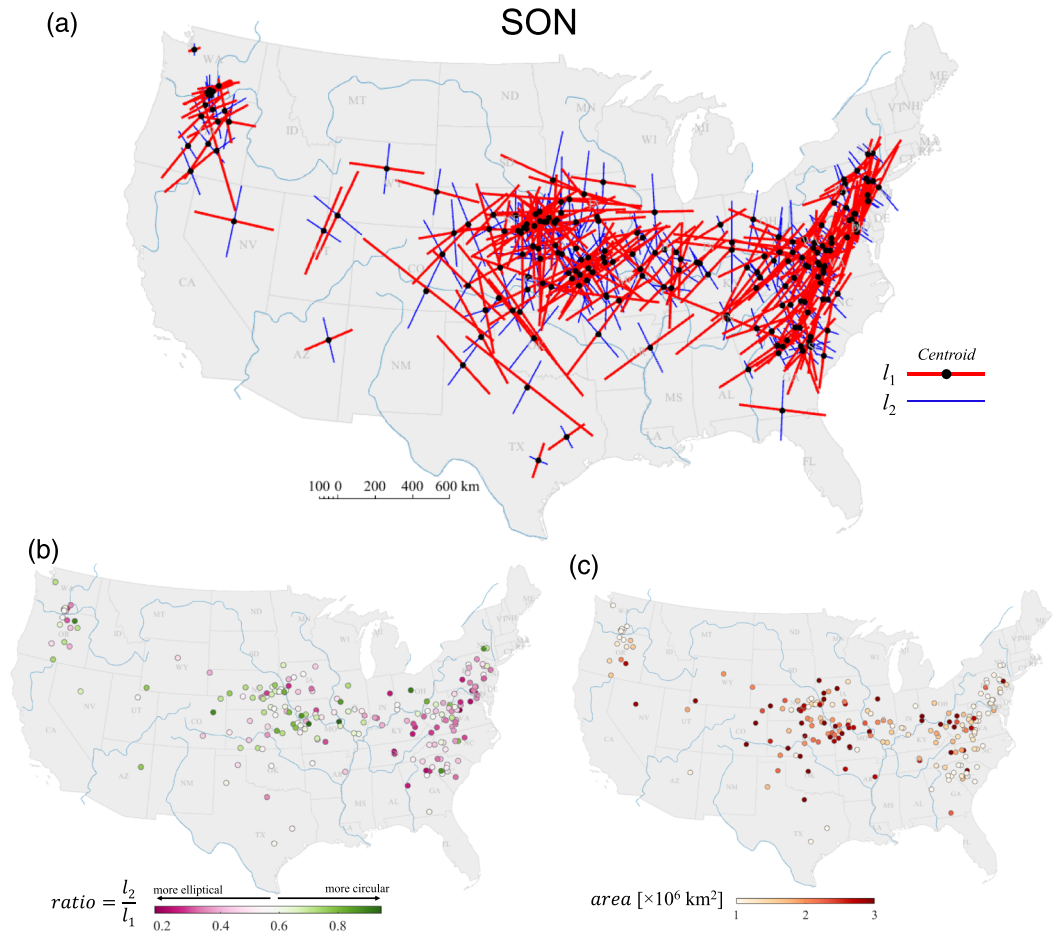
Figure 7. (a) Spatial distribution of SHPEs in the SON season shown using their centroids and stretches (l_1 and l_2 axes) (1900–2014), (b) distribution of l_2/l_1 ratio to indicate the elliptical and circular nature of SHPEs, and (c) areal extents of SHPEs (readers are cautioned against the projection artifact that might be influencing the orthogonality of l_1 and l_2 axes).

4.2.5. Summary of the Spatial Characteristics of Seasonal SHPEs

Figure 8 presents the distribution of the l_1 and l_2 axes (in kilommeters) as well as the orientation angles θ (in *degree*), in each season of DJF, MAM, JJA, and SON across the conterminous United States in 1900–2014. l_1 is the major principal axis, l_2 is the minor principal axis and θ is the orientation, derived from the eigenvalues and the eigenvectors of the coordinate vector.

In Figure 8a, the boxplots present the overall distribution of l_1 and l_2 in the DJF, MAM, JJA, and SON seasons. For all the seasons, l_1 and l_2 approximately vary between 400 and 2,000 km and from 100 to 1,100 km, respectively. l_1, the stretches (linear extents) of SHPEs over the major principal axis in the JJA season seem to be moderately longer than the stretches in the DJF, MAM, and SON seasons. Notice, for instance, that the median of l_1 in the JJA season is 1,250 km, compared to the other medians of 950, 1,150, and 1,050 km. The distributions of l_2, that is, the stretches along the minor axis (which is orthogonal to the major axis) seem to be approximately identical for the seasons of DJF and JJA (with medians of 572 and 574 km). Similarly, they seem to be identical for the seasons of MAM and SON (with medians of 493 and 509 km).

In Figure 8b, we present the distribution of θ, the orientation of SHPEs, for each season, as histograms. Attached to these histograms, we also show the data as horizontal boxplots. θ is mostly positive for SHPEs in the DJF and SON seasons indicating that the orientation of SHPEs in the DJF and SON seasons are primarily in the SW-NE directions. In the MAM and JJA seasons, there are SHPEs with positive and negative angles, in particular with slightly more frequent SHPEs in the SE-NW direction (negative angles) (see the median of distribution from the horizontal boxplots in Figure 8b for instance).
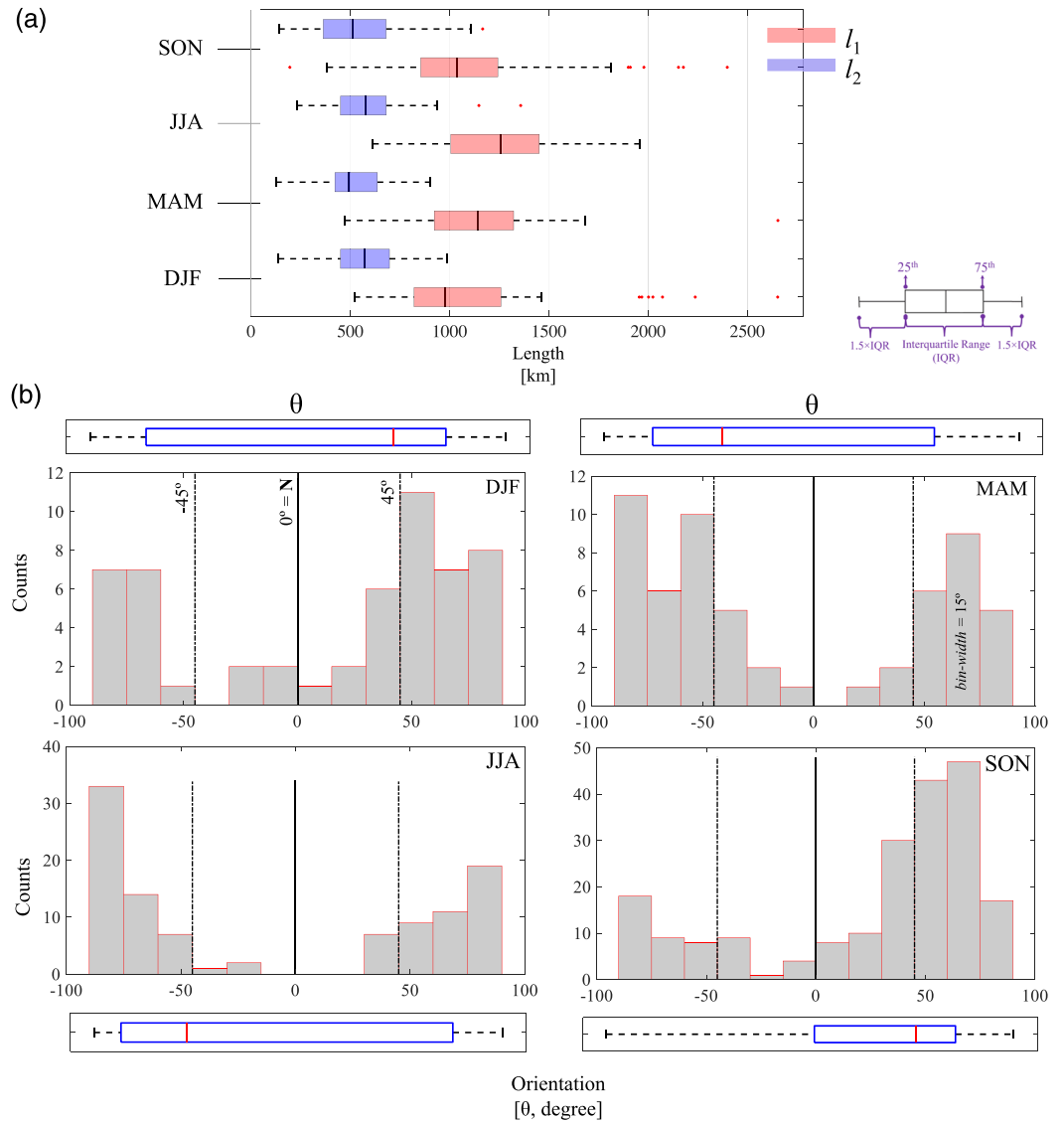
Figure 8. (a) Boxplots presenting the distribution of l_1 and l_2 axes of SHPEs, and (b) histograms indicating the number of SHPEs orientation angles (θ referenced to the geographical north) in each category (15° bin width). Horizontal boxplots in (b) show the overall distribution of θ in each of the DJF, MAM, JJA, and SON seasons across the United States (1900–2014). Positive and negative angles refer to the SW-NE and SE-NW orientations, respectively.

In addition to Figure 8, we provide Table 1 that summarizes the spatial characteristics of SHPEs in the four seasons during 1900–2014. To better comprehend the areal extents of SHPEs, we have also calculated its fraction with respect to the total area of the state of California (CA) which is 423,970 km^2 (163,696 mi^2) (US/Census/Bureau, 2012). For instance, if one considers the high-density area of SHPEs (i.e., inner ellipse in Figure 2b), the average areal extent of SHPEs in the DJF season is approximately 4.96 times the area of CA. It is 5.43 times the area of CA for the JJA season.

4.3. Identifying the Atmospheric Circulation Patterns for SHPEs

In addition to understanding the spatial manifestation of SHPEs and their geometric properties across the United States, we also examine the synoptic circulation for events that occurred in the same region and season. This analysis is meant to provide context for atmospheric conditions during the SHPEs. It is not meant to be an exhaustive analysis of the dynamics — such an analysis is outside of the main focus of this work. To provide context for the synoptic conditions, we present a compositing analysis that shows both the upper-level circulation and column water vapor. For our composites, we average together the daily

Table 1
Summary of the Spatial Properties of SHPEs That Occurred Across the United States in the DJF, MAM, JJA, and SON Seasons During 1900–2014

Attributes (average $\pm$ std)	DJF	MAM	JJA	SON
Number of SHPEs	54	58	103	204
l_1 (km)	$1,124 \pm 456$	$1,166 \pm 339$	$1,240 \pm 302$	$1,081 \pm 344$
l_2 (km)	568 ± 199	511 ± 156	579 ± 178	540 ± 216
l_2/l_1 ratio (km/km)	0.5435 ± 0.2009	0.4637 ± 0.1763	0.4861 ± 0.1621	0.5153 ± 0.1784
area (km^2)	2.104×10^6	1.897×10^6	2.303×10^6	1.930×10^6
area wrt CA[a] (l_1 , l_2)	4.962	4.474	5.431	4.615

[a]California has an approximate width, length, and area equal to 400 km, 1,240 km, and 423,970 km^2.

fields for dates on which a chosen set of SHPEs are centered; the choice of which SHPEs are explained below. The figures presented herein include the anomaly of the 500-hPa geopotential height field (Z_{500}) and the precipitable water vapor (PWV; the full field, not the anomaly). The Z_{500} anomaly is calculated with respect to the daily climatology (see section 2.2 for details). We chose these two fields because: (i) the Z_{500} anomaly captures the large-scale tropospheric circulation that is the backbone for the storms that generate the precipitation, and (ii) the full field for PWV displays moisture available. For PWV, we note that although it is a column integrated term most of the water vapor that makes of the column integral is found near the surface. As such, these composites provide an overview of the upper-level and near-surface conditions.

The first composite shown focuses on the 35 SHPEs during DJF in the Pacific Northwest region (see map of the SHPEs' locations in Figure 9a). These events are located primarily along the Cascade mountain range as well as the northern edge of the Sierras. The Z_{500} anomaly indicates that there is a trough to the northwest and a ridge to the southeast (Figure 9b). At 500-hPa the winds are approximately geostrophic, meaning they blow parallel to the isobars. Thus the anomalous upper-level wind is directed toward the SHPE impact region, and the low and high geopotential height anomaly pattern enhances the strength of the southwest to northeast flow. This upper-level synoptic pattern is indicative of extratropical cyclones that move into the Pacific Northwest region from the Pacific Ocean. The PWV shows a filament of moisture that extends from the subtropics (Figure 9b). The filament is directed along the same path as the anomalous upper-level winds. This pattern is consistent with the archetypical atmospheric river (AR) circulation that delivers the strongest precipitation events to the region (see more details in Gershunov et al., 2017; Guan et al., 2018; Huang et al., 2020; Jeon et al., 2015; Ralph et al., 2019; Waliser & Guan, 2017). As a reminder the composite include SHPEs that occur in the states of Washington and California and therefore the averaging used to generate the composite smooths the sharper features found in individual events.

The second composite is for the 74 SHPEs during JJA in the midwestern United States (see map of the SHPEs' locations in Figure 9a). This region is defined as all points east of 100°W and west of 86°W. 100°W demarcates the historical divide of the arid and wet regions of the United States, and 86°W separates the Midwest storms from the cluster seen throughout the Appalachian Mountains. This comprised watersheds that feed into the Mississippi River. In this case, the Z_{500} anomalies show a high-low-high wave-like pattern (Figure 9c). The pattern resembles a Rossby wave train, which has been attributed to other heavy precipitation events (Wang et al., 2013; Weaver & Nigam, 2008). The low heights anomaly is centered to the west, that is, upstream, of the precipitation events. The anomalous geostrophic circulation suggested by the Z_{500} anomalies includes wind blowing from south to north over the Mississippi river region. In this same region, the PWV is larger than the surrounding longitudes (Figure 9c), with the stronger values appearing to extend up from the Gulf of Mexico.

The third composite is focused on 85 SHPEs along the U.S. East Coast (see map of the SHPEs' locations in Figure 9a). These events occurred during SON and likely include tropical cyclones. However, the composite analysis suggests that for at least some of the SHPEs there is a strong upper-level trough involved as well. The Z_{500} anomalies show a pattern of high-low-high that is arranged in a V-shape with the low-heights anomalies at the bottom of the V. The lowest Z_{500} anomalies sit in the southern portion of the region of the SHPE locations and the highest Z_{500} anomalies are offshore north and east of the SHPE region (Figure 9d). In between this dipole in height anomalies, large values of PWV extend northward, seemingly following the
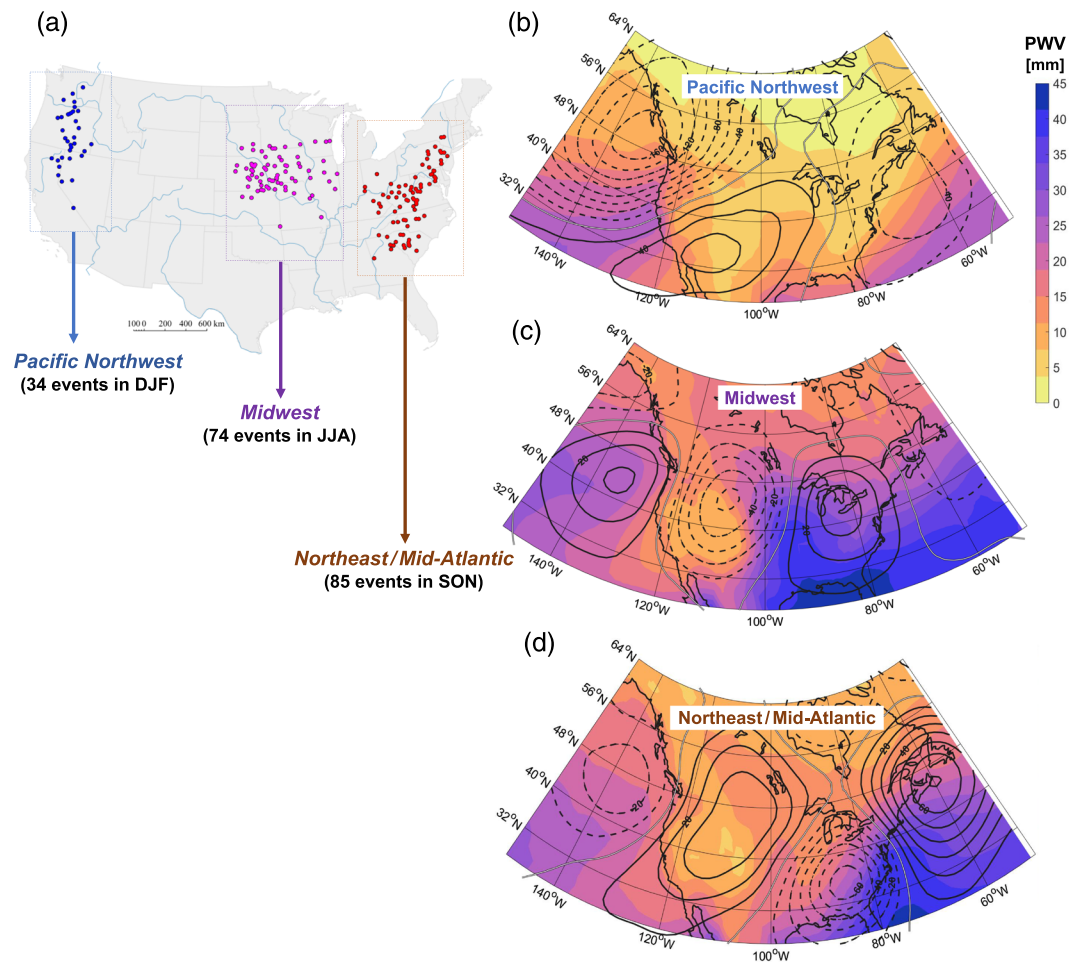
Figure 9. (a) Composite analysis: (a) Locations of the SHPEs used for composites. The right column shows composites of Z_{500} anomalies (contours) and PWV (shading) for (b) Pacific Northwest region during DJF (34 events), (c) Midwest during JJA (74 events), and (d) northeast/Mid-Atlantic during SON (85 events). Contour interval is 20 m in panel (b) and 10 m in panels (c) and (d). Dashed contours indicate negative height anomalies, and gray contour is the zero-anomaly line. Units for PWV are millimeters, and all three panels use the same color bar.

location of the Gulf Stream. The anomalous winds associated with the Z_{500} anomalies appear to be advecting the moisture inland.

The compositing analysis presented in Figure 9 both adds new information and affirms existing results. To our knowledge, no previous work has presented the composite circulation of precipitation extremes for these specific regions and seasons using a data set that spans over 100 years. Additionally, for the Midwest, the emergence of a zonal Rossby Wave-like pattern is a new result. However, given that the context of this paper is mainly the presentation of a new (spatially extreme) precipitation data set, the most important aspect of the compositing results are their affirmation of previous literature.

For the Pacific Northwest region in DJF (Figure 9a), the strong cyclonic anomaly northwest of the impact region is consistent with Loikith et al. (2017). Their self-organizing map analysis highlighted a similar pattern as the most likely to cause heavy precipitation. In our analysis and Loikith et al. (2017), the circulation suggests a strong extratropical cyclone tracking over the Cascade Mountain range into Canada with a cold front trailing to the south. This attribution of the extreme precipitation to the cyclones and fronts is consistent with the tabular results from the map analysis of contiguous United States precipitation extremes presented by Kunkel et al. (2012).

For the Midwest during JJA, Lavers and Villarini (2013) have shown that compositing SLP for all ARs leads to a low-pressure anomaly centered in the Midwest with high pressure anomalies to the west and east

(their Figure 5). In our analysis, a similar anomaly pattern emerges (Figure 9b), however the pattern is more zonal than Lavers and Villarini (2013). This is likely due to the fact that our cases are not exclusively limited to ARs. A compositing analysis of flood events (Nakamura et al., 2013) shows a similar pathway for the moisture fluxed northward into the Midwest region. Their work focused on events that exceed a 10-year return level for flooding and highlights a persistent, high pressure system northeast of the flood region. Our compositing analysis likely includes many more events that are weaker, and the Rossby Wave train in the upper-levels is more prominent than any persistent high pressure system.

For the northeast United States during SON, the Z_{500} anomalies identify a clear upper-level trough. These results agree with previous compositing work for the region which were based on tropical moisture exports (Steinschneider & Lall, 2015), summertime precipitation extremes in the northeast United States (Marquardt Collow et al., 2016), and precipitation extremes in farther north, in Newfoundland (Milrad et al., 2010). More recently, Agel et al. (2019) sorted northeast precipitation extremes by synoptic circulation — the patterns that created the strongest precipitation events look similar to those we find (e.g., their Clusters 2 and 6).

As an additional check, we compared the composites that use all dates with those using dates after 1 January 1979 (i.e., dates when ERA-Interim is available, since the ERA-Interim uses a more comprehensive data assimilation procedure), and the results are qualitatively very similar (not shown). Overall, the composite analysis provides a strong assurance that the algorithm used to identify SHPEs is properly capturing events in which the atmosphere was organized in a manner that can lead to heavy precipitation. The presence of an upstream trough and downstream ridge in the composites suggest that most of the events have strong upper-level forcing, and the presence of a filament of high PWV in each composite confirms that there was ample moisture available. For the Midwest and East Coast, there is a wave-like structure in the Z_{500} anomalies. The Midwest anomalies are aligned zonally, while the east coast anomalies create a trough structure with the low at the base of the trough. The Pacific Northwest stands out from the other two regions: It has the deepest upstream Z_{500} anomaly (note the different contour intervals as compared to the other two) and the smallest PWV amounts. The smaller PWV relates to the colder season and the lack of a warm ocean water in the near vicinity for this composite region. However, the stronger upper-level anomalies somewhat compensate for the weaker PWV amounts. That being said, one element for future work is the analysis of the propagation of the atmospheric circulation types, since the duration of the precipitation events is also critical for accumulation.

4.4. Quantifying the Spatial Manifestation of SHPEs

4.4.1. Frequency Distribution of the Areas of SHPEs

In this section, we attempt to quantify the frequency distribution of the areas of SHPEs using a power law distribution. Given our motive to eventually develop spatial flood risk models for civil infrastructure portfolio analysis, understanding whether the frequency of the observed SHPE areas follows an underlying theoretical distribution is of interest. Hence, for each season, we explored whether the empirical data of SHPE areas (as approximated by the ellipse) may be drawn from the power law distribution:

$$f(A) \propto A^{-\alpha} \text{ for } A > A_{\min} \tag{3}$$

where A_{min} is the threshold (lower bound) for the applicability of a power law and α is the scaling parameter or exponent, both of which are to be estimated from the data on SHPE areas (A) for each of the DJF, MAM, JJA and SON seasons, and $f(.)$ refers to the probability distribution for (.). The rate at which the frequency of SHPEs decays with increasing area is measured by α, the scaling parameter. We can also refer it to the slope of the SHPE area distribution. A large scaling parameter indicates fewer large-area SHPE events. In contrast, a smaller scaling parameter suggests a higher frequency of large-area SHPEs. A minimum area A_{min} is required for the power law to be admissible — events that lead to power law type distributions are most evident when the observations are greater than some threshold at the tail of the distribution. The scaling parameter may vary by the season reflecting different climate mechanisms described in section 4.3.

Scaling analysis (i.e., the identification of the scaling parameters of the power law or heavy tail distribution) of areal coverage of precipitation has been pursued in the past through analyses of event-driven information or satellite imagery products using relatively limited data records and for regional cases. Areal scaling of widespread extreme precipitation over longer durations that is contiguous at the continental scale has not been attempted. As seen from the results so far, SHPEs impact large areas. It is hence of interest to determine
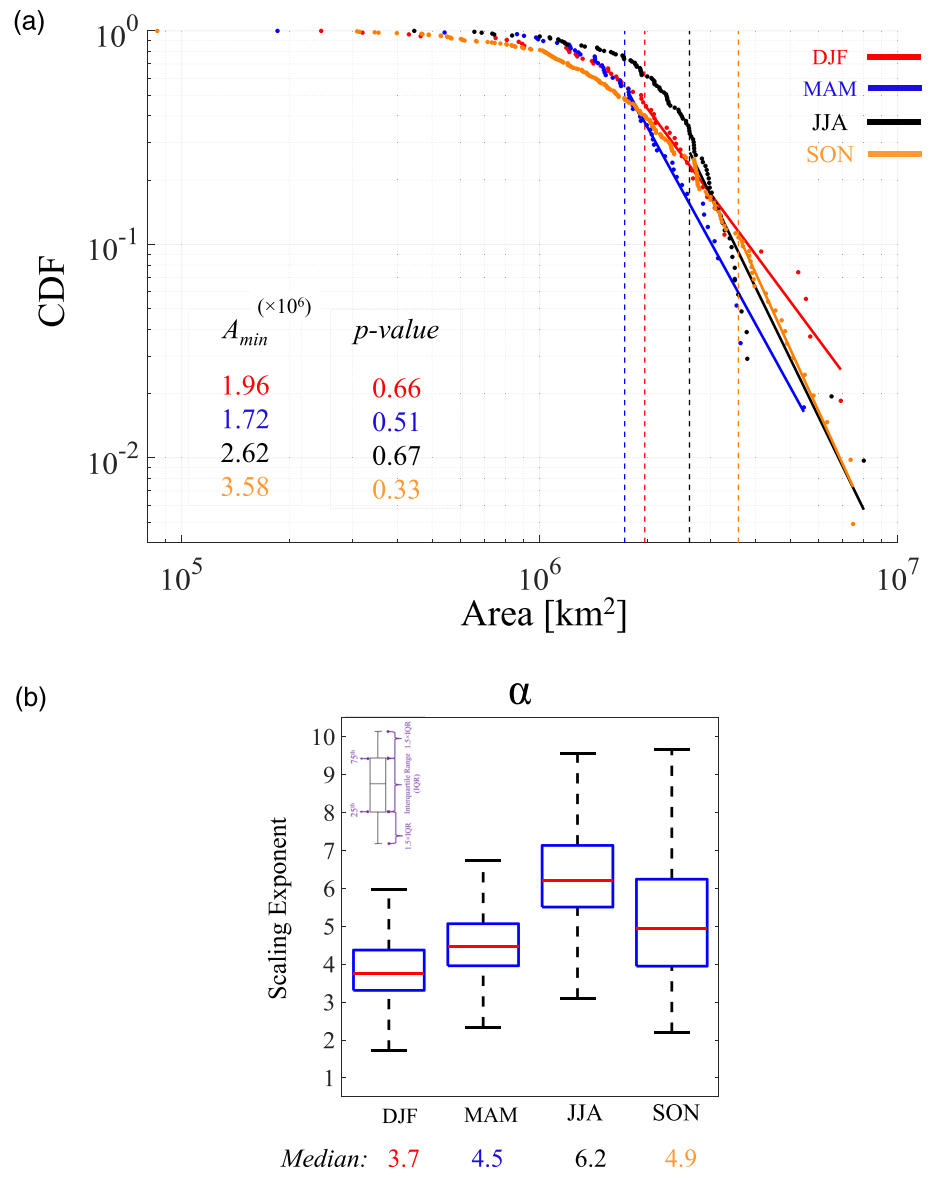
Figure 10. Results from the scaling analysis for the areas of SHPEs. (a) Solid-line indicates the power laws detected for areas of SHPEs. The associated p values from the bootstrap shown in the inset text. The dashed line refers to median A_{min}. The p values also show that the power laws cannot be rejected. (b) The distribution of the scaling exponents (α) for the DJF, MAM, JJA, and SON seasons with their median values.

the inherent scaling relations that will enable us to understand how unusual it is to have extreme precipitation footprints that large in nature. Previous studies in this line have empirically identified power laws for rainfall magnitude and areal coverage that explain the underlying self-organization and scaling behavior (Arakawa, 2006; Devineni et al., 2015; Dickman, 2003; Gupta & Waymire, 1993; Lovejoy, 1982; Rajagopalan & Tarboton, 1993; Sapozhnikov & Foufoula-Georgiou, 2007; Schertzer & Lovejoy, 1987).

For estimating the power laws, we chose to follow the approach developed by Clauset et al. (2009). Clauset et al. (2009) proposed a formal hypothesis testing based procedure to select A_{min} (i.e., the lower bound for the applicability of a power law), and to estimate α (the scaling exponent given A_{min}) using maximum likelihood. They also provide an approach to perform goodness-of-fit tests and generate a p value statistic based on a bootstrap resampling strategy to assess the probability that a power law distribution may be reasonable for a given data set. These steps are implemented using the "poweRlaw" package in the open source software R

(Gillespie, 2015). In our analysis, we used the continuous version of the algorithm with 5000 bootstrap samples. Interested readers can refer to Gillespie (2015) for details on the estimation procedure.

In Figure 10, we present the results. The complementary cumulative distribution function (or the survival function $P(A > a)$) of the data, the fitted power law, the p value for the significance of the power law fit for each season, and the median value of A_{min} is shown in Figure 10a. The box plots (sans outliers) of the scaling exponent selected across the bootstrap samples are presented in Figure 10b. A p value greater than 0.1 indicates that the null hypothesis, which states the power law is suitable for the data, cannot be rejected at the 90% confidence level, and the higher the p value, the higher the plausibility. This interpretation is consistent with Clauset et al. (2009) and (Gillespie, 2015). From Figure 10a, we can observe that power law appears to be suitable (p value >0.1) for all the seasons. A_{min} (in units of $10^6 \, km^2$) is varying from 1.72 to 3.58. For reference, $1.72 \times 10^6 \, km^2$ is approximately four times the area of California. Hence, power laws are admissible for SHPEs that have a sizeable areal extent. Given 54, 58, 103, and 204 SHPEs identified in the DJF, MAM, JJA, and SON seasons (1900–2014), there are 24 SHPEs (~45%) in the DJF season with an area greater than 1.96×10^6; there are 31 SHPEs (~53%) in the MAM season with $A > 1.72 \times 10^6$; there are 34 SHPEs (~33%) in the JJA season with $A > 2.62 \times 10^6$; and there are 21 SHPEs (~10%) in the SON season with $A > 3.58 \times 10^6$. It can hence be assumed that if there is a power law structure to SHPEs, it may be at significantly larger spatial scales, and, the DJF and MAM seasons seem to have a higher percentage of SHPEs that exhibit this self-organization. For JJA and SON, the threshold (A_{min}) areas are much higher than the DJF and MAM seasons, indicating that in JJA and SON seasons, the scaling manifests only for significantly large SHPEs.

Based on the magnitude of the p value, the most reliable results are the DJF and MAM seasons. All the seasons have a median scaling exponent (α) greater than 3, indicating a finite first and second moment (i.e., a well defined mean and variance) for the power law distribution (Newman, 2005). They range from 3.7 to 6.2. Based on the distribution of α, we can say that the scaling exponents for the DJF and MAM are comparable and lower, while the JJA and SON seasons have higher values for α. We can also see this from the slopes of the fitted lines shown in Figure 10a. The slope (or the scaling parameter) of the fit for DJF is smaller than the other fitted lines. However, α values for the JJA and SON seasons have more uncertainty. A lower scaling exponent indicates a higher frequency of large-area SHPEs, or, a higher probability of exceedance for tail events. A different way of interpreting the scaling exponent is that it is the rate of change of the exceedance probability (survival function, $P(A > a)$) with the change in the areal extent. A lower value indicates a slower decay, or asymptotic convergence, a fatter tail in the distribution of the areas, and hence more likelihood for large areal extent events. Depending on the antecedent soil states and the orientation of the drainage network of the terrestrial hydrologic system, these large SHPE areal events can cause significant flooding. SHPEs in the DJF and MAM seasons are prime candidates for this phenomenon. DJF and MAM are also the seasons during which the midlatitude jet stream is persistent in time, and, in conjunction with the atmospheric blocking phenomenon (Booth et al., 2017; Pfahl & Wernli, 2012), enables the delivery of extreme moisture over relatively large contiguous areas.

In summary, while power law seems to be suitable to explain the underlying scaling behavior for SHPEs in all the four seasons, based on the values of A_{min} and α and the p value, the SHPEs in DJF and MAM seem to show a stronger evidence for such self-organization. A thorough investigation into the physical processes leading to such large-scale organization, that is, how does the climate system organize over these scales, is required to understand their causality.

4.4.2. Inference and Prediction of the Spatial Risk

In the previous section, we attempted to quantify the frequency distribution of the areas of SHPEs using power laws. In this section, we develop a statistical model for the inference and prediction of the spatial risk of SHPEs in each season. We quantify risk using the "probability that a given location will be the centroid of an SHPE." In other words, what is $P(Y_i = \text{Centroid}_{shpe})$, where Y_i is the spatial coordinate vector, [lon, lat] for each i, the 1,244 GHCN-D stations. Location can be a GHCN-D station, as in this case, or a homogenized spatial grid. We explored a minimum number of covariates in geographic and meteorological predictors for this inference and prediction. Information about the longitude, latitude, and elevation are the chosen geographic covariates. Long-term meteorological phenomena summarized by the mean and coefficient of variation of the integrated water vapor transport (IVT) are chosen as the meteorological predictors (i.e., IVT_{mean} and IVT_{cv}). IVT is the integral of the moisture flux and pressure in the entire atmosphere layer, thus aggregating the information of winds and PWV. Since we observed pronounced large-scale atmospheric

behavior during SHPE days (see the discussions in section 4.3), we chose to use *IVT* derivatives as the mete-orological covariates that can explain and predict the centroids of SHPEs. *IVT* has been used previously as an explanatory variable to understand heavy precipitation, large-scale moisture intrusions to the land, and ARs (Khouakhi & Villarini, 2016; Lavers & Villarini, 2015; Mahoney et al., 2016; Neiman et al., 2008; Zhang & Villarini, 2018; Pan & Lu, 2019). The purpose of this inference and prediction scheme is to create a model that accurately identifies the chance of any location in the United States being the centroid of an SHPE. We will hence be able to predict the central location of the high-risk regions associated with SHPEs for each season. This, together with the auxiliary information about the major and minor principal axes, orientation and areas can be used to simulate the spatial extents. The details of the model are presented next.

First, for each season, we have taken the corresponding SHPEs and assigned their Centroid$_{shpe}$ to a nearest GHCN-D station. Note that since the centroid of an SHPE is the joint first moment computed from the vector of the spatial coordinates, it does not have to be a physical station. By assigning the Centroid$_{shpe}$ to its nearest GHCN-D station, we are creating measurable geographic covariates (longitude, latitude, and elevation) for training the model. Each of these stations —"adjusted centroids"— will also be assigned a binary indicator 1 to register the occurrence of an SHPE; that is, the station is now the center of an SHPE. The remaining GHCN-D stations will be assigned a value of 0 as a token for nonoccurrence of an SHPE; the other stations are not the center of any SHPE. Hence, we now have a dependent variable *Y* as a binary indicator for each of the 1,244 stations, and three geographic covariates for each station —their longitudes (*lon*), latitudes (*lat*) and elevations (*elev*). As mentioned above, we did this data preparation for each of the four seasons. Since the DJF, MAM, JJA and SON seasons have 54, 58, 103 and 204 SHPEs, respectively, the upper bound on the number of "ones" in the dependent binary variable *Y* is 54, 58, 103 and 204 for each season. The number of "ones" in *Y* for a season is not equivalent to the number of SHPEs in that season since multiple events can be assigned to the same nearest stations. After assigning the nearest station as the "adjusted centroid" for each of the events, we have 40, 57, 91 and 171 "ones" in the DJF, MAM, JJA, and SON seasons.

Next, we calculated the long-term average (*mean*) and coefficient of variation (*cv*) of the daily vertically Integrated Water Vapor Transport (IVT) for the 1850–2014 period (165 years) for each $2° \times 2°$ grid over the United States. To compute IVT_{mean} and IVT_{cv} metrics, we collected 165 years of daily specific humidity (S_H), component vectors of wind (*V*; horizontal and vertical components as *u* and *v*, respectively), and geopotential height fields. These records (provided by the NOAA/CIRES V2c Reanalysis data set (Compo et al., 2011)) are obtained along 15 pressure levels between the Earth's surface ($P_{surface} = 1,000$-hPa) and 300-hPa. We computed *IVT* according to the following formula:

$$IVT = \frac{1}{g} \int_{P_{surface}}^{300} q.Vdp = \frac{1}{g}\sqrt{\left(\int_{P_{surface}}^{300} q.udp\right)^2 + \left(\int_{P_{surface}}^{300} q.vdp\right)^2} \tag{4}$$

where *q* refers to specific humidity (S_H, kg/kg), *V* to wind vector [m s^{-1}], *dp* to the pressure difference between two adjacent vertical levels, and *g* to the acceleration induced by gravity (9.81 m s^{-2}). The daily *IVT* values (kg m^{-1} s^{-1}) are calculated at $2° \times 2°$ spatial resolution globally for the period of 1850–2014. For each grid, we then summarize this daily data using the mean and coefficient of variation (i.e., the standard deviation relative to the mean) for the four seasons separately. The 1,244 GHCN-D stations then get these two additional meteorological covariates for each of the DJF, MAM, JJA and SON seasons through a standard search, in which GHCN-D$_{[lon,lat]} \in IVT_{[lon,lat]}$. In simple terms, we locate the grid that the GHCN station is part of, and assign the seasonal IVT_{mean} and IVT_{cv} of that grid to this GHCN station. Due to the wider spatial resolution of the *IVT* mesh grid, multiple GHCN-D stations part of the same grid get the same IVT_{mean} and IVT_{cv} values. Ultimately, each station from the list of 1,244 stations will have the IVT_{mean} and IVT_{cv} values in each of the DJF, MAM, JJA, and SON seasons.

We model ***Y*** as a Binomial distribution whose probability ($P(Y_i = 1)$) is estimated using an inverse logistic function on a possible set of linear additive covariates described above. $Y_i = 1$ indicates that station *i* is the centroid of an SHPE, and $Y_i = 0$ indicates otherwise.

$$Y_i \sim Binomial\left(p_i\right)$$
$$logit(p_i) = \delta + \beta_1 lon_i + \beta_2 lat_i + \beta_3 log(elev_i)$$
$$+\beta_4 IVT_{mean_i} + \beta_5 IVT_{cv_i}$$
or
$$P(Y_i = 1) = logit^{-1}\left(\delta + \beta_1 lon_i + \beta_2 lat_i + \beta_3 log(elev_i)\right)$$
$$\left(+\beta_4 IVT_{mean_i} + \beta_5 IVT_{cv_i}\right) \tag{5}$$

Table 2
Summary of the Stepwise GLM for Quantifying the Probability That a GHCN-D Station Will Be an SHPE Centroid

$\delta + \beta_1 lon + \beta_2 lat + \beta_3 log(elev) + \beta_4 IVT_{mean} + \beta_5 IVT_{cv}$

Coefficients	DJF	MAM	JJA	SON
δ	−30.253** (4.127)	−20.749* (5.094)	−29.905** (5.635)	−20.231** (3.713)
β_1	−0.101** (0.022)	—	−0.107** (0.031)	−0.0435** (0.016)
β_2	—	0.290** (0.088)	−0.193** (0.059)	−0.058* (0.023)
β_3	1.131** (0.242)	0.588* (0.265)	0.376* (0.183)	0.700** (0.136)
β_4	0.204** (0.044)	0.253** (0.058)	0.405** (0.062)	0.311** (0.053)
β_5	6.345* (2.498)	−8.035** (2.798)	16.966** (4.432)	4.645** (1.599)
AIC	260.81	404.06	568.99	902.64

Note. The spatial covariates are the coordinates (longitude and latitude) and elevation information (meters above mean sea level (MSL)) as well as Integrated Water Vapor Transport (IVT). Results from the four seasons are shown in separate columns. Values in parentheses denote the standard errors. '—' indicates that the covariate is not selected in the stepwise GLM.
*p value <0.05. **p value <0.001.

In Equation 5, Y_i is a vector of "ones" and "zeros" indicating whether or not the station was the "adjusted centroid." δ, β_1, β_2, β_3, β_4, and β_5 are the coefficients for the regression model (i.e., scaling factors of the geographical and meteorological predictors). We used the stepwise generalized linear regression model (GLM) framework with a logistic link function (Dobson & Barnett, 2008) to estimate the regression coefficients and identify the best subset predictors. Stepwise regression is a systematic method for adding and removing the existing terms from the formulated GLM based on their statistical significance in explaining the response variable ($logit(p_i)$ here). The summary of the stepwise GLM is presented in Table 2.

In Table 2, the estimated regression coefficients, their standard errors and the level of statistical significance (at 0.001 or 0.05 level), as well as the Akaike information criterion (AIC) (Akaike, 1974) for the final model are presented for each of the DJF, MAM, JJA, and SON seasons. Based on the results from the stepwise GLM, it is evident that the station elevation and the two meteorological covariates, IVT_{mean} and IVT_{cv} are significant and useful in explaining the probability that a location will be the centroid of an SHPE, for all the four seasons. Longitude is a significant covariate for the DJF, JJA and SON seasons, and latitude is a significant covariate for the MAM, JJA and SON seasons.

For the DJF season, we find that the longitude covariate has a negative coefficient, while elevation, IVT_{mean}, and IVT_{cv} have positive coefficients. We hypothesize that the positive coefficient for the elevation covariate (which indicates that there is a greater probability for stations in higher elevations to be the centroids when other covariates are held constant) is due to the interaction of orographic barriers such as the mountainous terrain of Sierra Nevada and Coast Ranges with moisture transport to the region, causing enhanced large-scale uplift and heavy downpours (e.g., see Galewsky & Sobel, 2005; Jiang, 2003; Leung et al., 2003; Pandey et al., 1999). Latitude is not a significant covariate. For simplicity, we follow the "divide by 4 rule" suggested by Gelman and Hill (2006) to interpret the regression coefficients in terms of the maximum difference in $P(Y_i = 1)$ corresponding to a unit difference in one covariate, while others are unchanged. Accordingly, for the DJF season, $P(Y_i = 1)$ decreases by 3% as we move west to east (unit increase in the longitudinal direction, that is, 1° ~110 km), increases by 28% as we move up in altitude (elevation units of 1 m), increases 5% with a unit increase in the mean value of IVT and increases by 158% with a unit change in the variance of IVT.

For the MAM season, $P(Y_i = 1)$ increases by 7% as we move south to north (unit increase in the latitudinal direction, i.e., ~110 km), increases by 15% as we move up in altitude (elevation units of 1 m), increases by 6% with a unit increase in the mean value of IVT and decreases by 200% with a unit change in the variance of IVT.

For the JJA season, $P(Y_i = 1)$ decreases by 3% as we move west to east, decreases by 5% as we move south to north, increases by 9% as we move up in altitude, increases by 10% with a unit increase in the mean value of IVT and increases by 424% with a unit change in the variance of IVT.
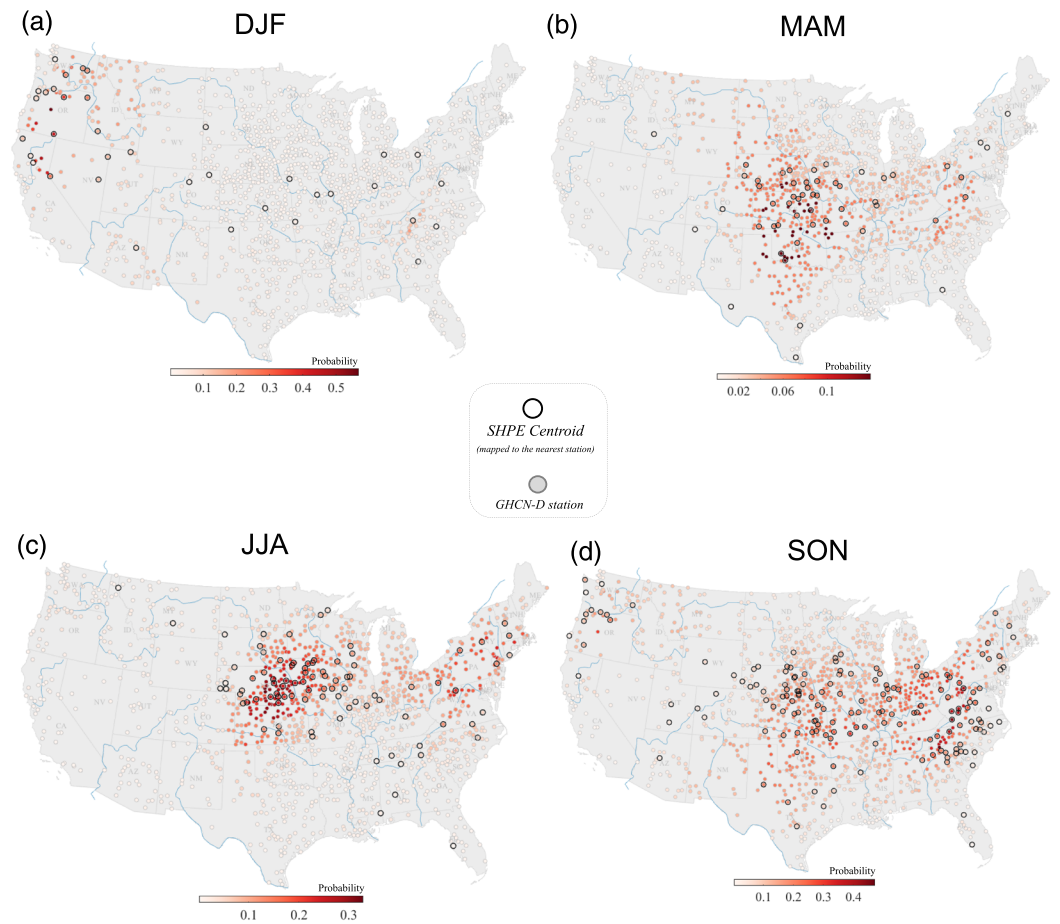
Figure 11. Probability of any station being the centroid of an SHPE as derived from the inference model for the (a) DJF, (b) MAM, (c) JJA, and (d) SON seasons. The centroids of SHPEs calculated from the precipitation observations are adjusted to their nearest stations and overlaid on the map as hollow circles.

Finally, for the SON season, $P(Y_i = 1)$ decreases by 1% as we move west to east, decreases by 1% as we move south to north, increases by 18% as we move up in altitude, increases by 8% with a unit increase in the mean value of IVT and increases by 116% with a unit change in the variance of IVT.

When we compare these changes across seasons, we find that the change in $P(Y_i = 1)$ is around 2% with change in longitude, between 1% and 7% with change in latitude (with MAM having the largest change of 7%), between 9% and 28% with change in elevation, between 6% and 10% with change in IVT_{mean} and between 116% and 425% with change in IVT_{cv}. It is interesting to note that, for elevation, the most significant change is seen in the DJF and SON seasons where much of the SHPEs are geographically aligned to the Rocky Mountains in the west and the Appalachian in the east. SHPEs in the MAM and JJA seasons are mostly distributed in the plane lands, and their changes are lower than the changes in the mountainous regions. Further, we see that $P(Y_i = 1)$ is sensitive to the spatial difference in IVT_{cv} with the most significant effect in the JJA season.

Following the construction of the logistic regression models for each season, we have estimated probabilities for every single GHCN-D station using the inverse logistic function on the model selected covariates. This process results in the derivation of the likelihood that a station will be the centroid of an SHPE. Figure 11 presents these results for each of the four seasons.

In Figures 11a–d, the black-colored hollow circles indicate the locations of the "adjusted centroids" of SHPEs. The color-bar in Figure 11 shows the probability $P(Y_i = 1)$ as predicted from the logistic model. Darker red-colored shades refer to a higher probability that the station will be an SHPE centroid. Based on the comparison (see the majority of stations would get a higher $P(Y_i = 1)$) when they are neighboring or
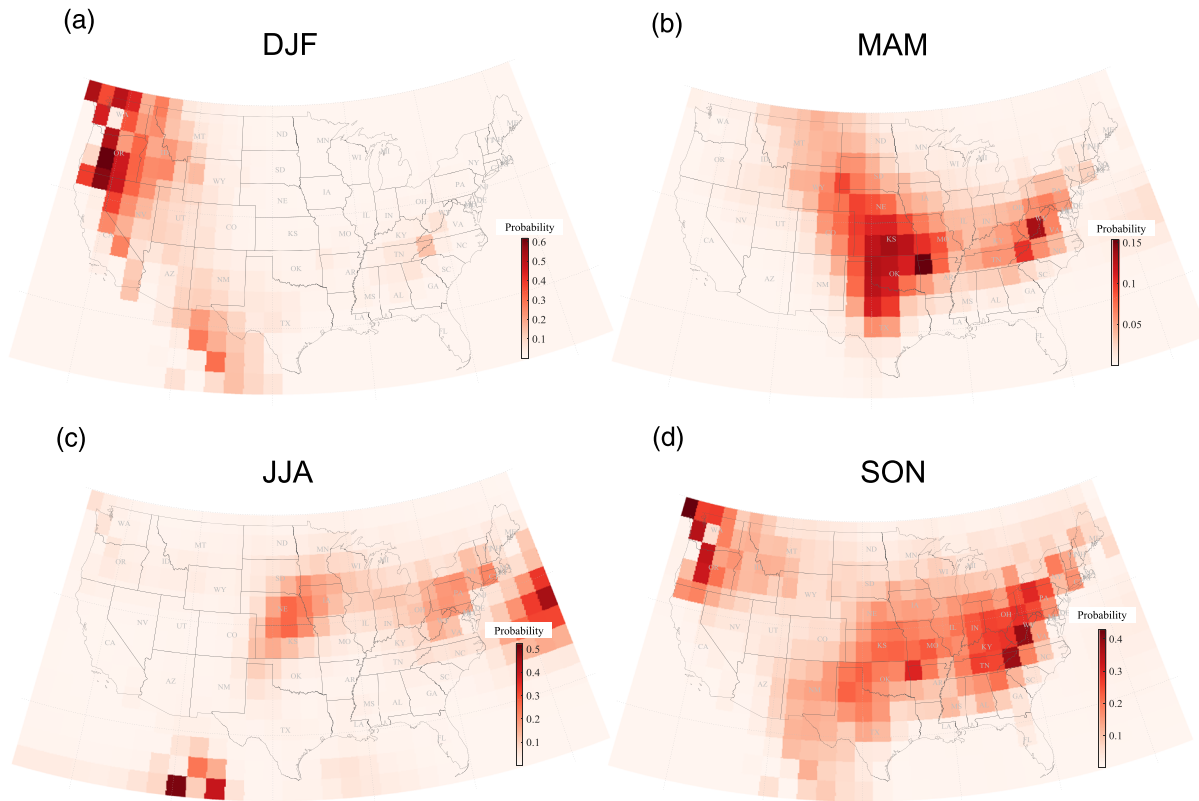
Figure 12. Predicted probability of any grid (2° × 2°) being the centroid of an SHPE based on the spatial risk model for the (a) DJF, (b) MAM, (c) JJA, and (d) SON seasons. The darker shaded areas indicate a higher chance of SHPE risk.

near an SHPE centroid), we can presume that logistic regression model returns accurate predictions in all four seasons. It should also be noted that the model's identifiability also improves with the increase in the density of the centroids.

4.4.3. Assessing the Robustness of the Model and Predicting the Spatial Risk

We have conducted a leave-k-out cross-validation strategy to examine the robustness of the model before we apply it for predicting the spatial risk of SHPEs at the United States level.

For each season, we randomly select and leave out 10% of the 1,244 GHCN-D stations (i.e., 125 stations), train the model (Equation 5) using the remaining 1,119 stations, and then predict $P(Y_i = 1); \forall i \in (1, 2, \ldots, 125)$. In other words, for the 125 left out GHCN-D stations, we predict their probability of being a centroid, using the trained model. From this predicted $P(Y_i = 1)$ for each of the 125 stations, we draw a random trail (0 or 1) from a Bernoulli distribution to indicate whether or not that station is the centroid of an SHPE. Next, we compute the proportion of these predicted centroids in the 125 stations; $p_1 = \frac{\#\text{of predicted 1s}}{125}$. We also com-pute the observed proportion of actual centroids from the 125 left out samples; $p_2 = \frac{\#\text{of predicted 1s}}{125}$. An error metric as the difference between the observed and the predicted proportions is computed; $e = p_1 - p_2$. This procedure is repeated 1,000 times to obtain the null distribution of the error metric. We verified the null dis-tribution of the error against zero error using a standard t-test and found that the null hypothesis that the error is 0 cannot be rejected (at the 10% confidence level) for all the four seasons.

Besides the error metric on the overall proportion of predicted centroid, we also verified the model results using a much more stringent measure, the hit-rate. As before, for the 125 left out GHCN-D stations, we predict their probability of being a centroid using the trained model on the 1119 stations. From this predicted $P(Y_i = 1)$ for each of the 125 stations, we draw a random trail (0 or 1) from a Bernoulli distribution to indicate whether or not that station is the centroid of an SHPE. We compute hit-rate as the fraction of total "ones" among the real id in the 125. In other words, in a random sample, if there are m centroids, we verify what fraction of m the model can predict accurately. We repeat the Bernoulli draws 100 times and take an expected hit-rate. The leave-10%-out cross-validation procedure itself is repeated 1,000 times to obtain the

distribution of expected hit-rate across multiple randomly left out samples. For all the seasons, the mean of the distribution of the hit-rate ranges between 7% and 17%, and the maximum of the distribution ranges between 14% and 63%. It has to be noted that the hit-rate we are computing inspects for an exact match of the station without any scope for spatial errors. Hence, it is a highly conservative measure. We also found that the nonoccurrence hit-rate is above 90% in all seasons, indicating that the model structure is also sufficiently robust in avoiding false alarms.

Finally, we provide predicted gridded spatial risk maps based on the models for each season. To do so, we applied the logistic model on the longitudinal and latitudinal coordinates and elevation information as well as the IVT_{mean} and IVT_{cv} for the gridded IVT mesh over the United States in each season. We considered the center of each $2° \times 2°$ grid as the coordinates for the longitude and latitude. We extracted the elevation (in meters) at $0.125°$ resolution from the GMTED2010 (Global Multi-resolution Terrain Elevation Data) with respect to the geoid WGS84, provided by the U.S. Geological Survey (Danielson & Gesch, 2011). Given the longitudes and latitudes of the IVT grid, we assigned the nearest elevation information available in the GMTED2010 gridded mesh data to the corresponding IVT grid. Figure 12 presents the final gridded spatial risk maps in terms of the chance of each grid cell being the centroids of the SHPEs in each DJF, MAM, JJA, and SON seasons.

There are grid cells in each panel of Figure 12 featuring darker shades of red colors. The darker patterns indicate that a higher probability is associated with those grid cells for observing the centroids of SHPEs over this region. Considering Figures 11 and 12 in conjunction, one can realize that the SHPE risk model for each season can accurately reveal the centroids for SHPEs over the United States. The shaded regions with darker red-colored pattern can entirely depict similar spatial patterns with respect to the discrete points that we presented earlier in the Results section (i.e., in section 4, Figures 4–7 and 11). Hence, we summarize that the model formulation is robust, and the model performance is reliable for each of the DJF, MAM, JJA, and SON seasons across the conterminous United States.

5. Summary and Conclusions

This study presents a new way of quantifying the spatial manifestation of extreme precipitation. We introduce SHPE —*simultaneous heavy precipitation event*— to understand the daily compound effects of the spatially oriented extreme precipitation events (>99th percentile) for each of the DJF, MAM, JJA, and SON seasons across the conterminous United States (1900–2014). The spatiotemporal characteristics of SHPEs are assessed to discern their properties in different seasons. Their spatial manifestations are quantified using power laws for areal extents and inverse logistic functions for the probability of centroids. Ultimately, these models can be used as a basis for several floodplain management strategies and reliability analyses of the infrastructure systems.

We analyzed a high-quality data set of 1,244 daily GHCN-D precipitation observations distributed throughout the United States starting from 1 January 1900 to 31 December 2014 and found that there are 54, 58, 103, and 204 SHPEs in the DJF, MAM, JJA, and SON seasons. We identified the centroids and lateral stretches for these SHPEs and thus quantified them as quasi-elliptical. Then, we briefly explained the synoptic circulation patterns, including the Z_{500} anomalies and PWV fields corresponding to the selected SHPEs in over the U.S. Pacific Northwest, the Midwest, and along the East Coast. To predict the spatial risk, we also developed a statistical inference model that utilizes the spatial coordinates with elevation information, as well as average and coefficient of variation obtained from the historical IVT values over the United States. We examined the robustness and performance of the developed model using a leave-*k*-out cross-validation technique. Next, we adopted this predictive model for individual seasons and applied it to IVT gridded data and presented the estimated spatial risk manifestation in each of the DJF, MAM, JJA, and SON seasons nationwide.

The summary and concluding remarks related to the spatial manifestation of SHPEs are as follows:

1. Between 1900 and 2014, there was no significant trend in the annual frequency of SHPEs that occurred throughout the United States. However, we found a quasi-convex behavior of the long-term mean with slightly increasing frequency in the second half of the 20th and early 21st centuries. On average, three to four SHPEs occurred each year.

2. In the DJF season, a majority of SHPEs are manifested in the Cascade Range and the U.S. Pacific coast region as circular shapes (a rounded spatial footprint with l_2/l_1 *ratio* close to 1). The major axes of SHPEs

(i.e., l_1) are mostly between 650 and 1,500 km and oriented in the SW-NE direction. SHPEs in this season also have the least frequency of occurrences in 1900–2014, but they have maximum variations in terms of the second axis of SHPEs (l_2) relative to the other three seasons.

3. SHPEs in the MAM season are mostly manifested in the central to south central United States with a few SHPEs along the northeast belt. The l_1 length ranges mostly from 850 to 1,600 km. The orientation of SHPEs in the MAM season is in both SW-NE and SE-NW directions (the median of the distribution of θ shows a small negative angle referring to the SE-NW direction). SHPEs located in the central United States have more circular manifestations with larger areas compared to those along the U.S. northeast.

4. The 103 SHPEs that occurred in the JJA season have the largest areas and longer spatial axes (950 to 1,550 km) on average. They are mostly manifested in the U.S. Midwest and the East Coast. The majority of SHPEs that occurred across the Midwest indicates a mixture of circular and elliptical formations, while those in the East Coast represent elliptical manifestation. The orientation of SHPEs in this season is along both SW-NE and SE-NW directions with slightly more SHPEs with a SE-NW orientation.

5. The maximum number of SHPEs during the 1900–2014 period occurred in the SON season with 204 SHPEs (~50% of total) and three spatial clusters over the U.S. West Coast, the Midwest, and the northeast regions. SHPEs in the Midwest have mostly circular formations, while those in the northeast indicate elliptical configurations on the ground. Most SHPEs in the SON season are orientated in the SW-NE direction and l_1 has a median of 1,050 km derived from the distribution of the entire 204 SHPEs. We also realized that several SHPEs with larger areal extents were manifested in the Midwest cluster of the SON season.

6. We used compositing analysis to confirm that the SHPEs found were associated with the expected large-scale atmospheric circulation patterns. For the Pacific Northwest in DJF, the Midwest in JJA, and the northeast/Mid-Atlantic in SON, the composites show upper-level troughs or wave-like structures that could support storm development, or at the least would organize the low-level moisture that is found in PWV composites.

7. We examined the self-organization structure and potential scaling process of the areas of SHPEs and found that for all seasons, the frequency distribution of the areas of SHPEs can be explained using power laws. SHPEs in the DJF and MAM seasons show more evidence of self-organization. The results showed that ~45%, ~53%, ~33%, and ~10% of SHPEs in the DJF, MAM, JJA, and SON follow the power law structure. These SHPEs have substantially larger spatial scales.

8. In addition, we modeled the spatial risk of SHPEs in each season using a logistic regression model. We developed an inference (and predictive) model that can be used to estimate the probability of SHPE centroid for any geographical location across the United States using spatial (longitude, latitude, and elevation) and meteorological (the mean and the coefficient of variation of *IVT*) predictors. *IVT* captures the dynamics of water vapor, pressure systems, and wind variabilities inside a column of the atmosphere, and hence, serves as a good meteorological covariate. Results indicate that the parsimonious model with minimum covariates can be used to accurately quantifying the centroids of SHPEs in each DJF, MAM, JJA, and SON seasons. In particular, the average of historical *IVT* and its coefficient of variation, as well as the elevation information happen to be the most statistically significant predictors in quantifying the spatial manifestations of SHPEs in all seasons. We used the trained model on a fully gridded data set of predictors and presented the probabilistic spatial risk maps corresponding to the centroids of SHPEs. These seasonal risk maps show the probability of each spatial location (longitude and latitude) on the ground in the United States being the center of extreme precipitation events.

The synoptic patterns derived in our compositing analysis (Figure 9) affirm previous work (e.g., Agel et al., 2019; Loikith et al., 2017; Marquardt Collow et al., 2016), which is a combination of a strong upper-level wave and near-surface moisture convergence are the most common elements of the atmosphere that are required for generating heavy precipitation events in the midlatitudes, in the absence of a tropical cyclone. From case studies, we know that there are important subtleties in any storm that can have big impacts on the precipitation amount, and these are often averaged out in composites. However, knowing the most likely synoptic-scale organization of the atmosphere is a critical first step in fully understanding the physics of these extreme precipitation events.

The spatial patterns, climate mechanisms and the spatial risk models for the United States provide essential insights for understanding the spatial manifestation of widespread extreme precipitations on the ground. The findings and models discussed in this work can be directly used by floodplain managers, insurance

agencies, and reservoir operators. For example, one can quantify the vulnerability of residential structures and infrastructure systems that are geographically under or adjacent to SHPEs and then report the probabilistic exposure to heavy precipitation in each season. The SHPE derivations we presented in this work provide a new path to analyze the footprints of heavy downpours associated with the different rainstorm systems at the local to global scales. The SHPE database will benefit the entire hydroclimatology community ranging from reservoir managers and local governments to earth system scientists and climate change researchers. The uniformness of the analysis and availability of the database countrywide improves upon and complements other regional-scale studies in this direction.

For hydrologists, the SHPE database provides a unique tool to explore and predict the spatial extent of large river floods. It is also important to explore whether the current generation of global circulation models adequately represents the spatial features depicted in these ground-based measurements, and how they could be improved to describe these spatial features better. Our analysis also provides a pathway to explore whether phenomena such as the ENSO, Pacific Decadal Oscillation, and North Atlantic Oscillation translate into patterns of organization in the tropics and extratropics that eventually lead to large areas associated with extreme rainfall showing a specified geographic character.

In closing, we would like to point out that we also validated the number of identified SHPEs using a gridded product (see Appendix A) and demonstrated that there is no significant difference in the identified SHPEs between those from the ground-based data set and the gridded data set. Further, it should also be noted that the algorithm is generalized enough to take in different values for the extreme rainfall threshold and RoE threshold. A lower extreme rainfall threshold will allow for the analysis of less intense events, and a lower RoE threshold will yield more SHPEs (see Appendix B). The SHPE database can serve as input training data for modern machine learning algorithms to detect more intricate spatiotemporal patterns. Further investigations are required to accurately quantify the spatial manifestation of smaller storm events and coastal-oriented events that are influenced by land-ocean contrast or limited availability of data records. These are some of our main research tracks to address in the near future.

Appendix A: Validating SHPEs Using Gridded Precipitation Data

A1. Gridded Precipitation Data: CPC Unified Gauge-Based Daily Precipitation

To ensure that our findings are not influenced by the sparse network of ground-based rain gauges, we also corroborated them with the results obtained from applying the SHPE detection algorithm on the daily gridded precipitation data from the NOAA Climate Prediction Center (CPC) Unified Gauge-Based Analysis of Daily Precipitation over the CONUS (Xie et al., 2007). NOAA/OAR/ESRL PSD (Boulder, CO) provides the CPC daily U.S. Unified Precipitation data. The CPC unified gauge-based daily precipitation database has a $0.25° \times 0.25°$ spatial resolution over the United States (and $0.5° \times 0.5°$ at the global scale) that extends from 20.125–49.875°N and 230.125–304.875°E. Hence, it provides a daily grid of precipitation data (a matrix with a dimension of 300×120 (longitude, latitude)) over the United States since 1948. We have processed and organized 67 years of daily gridded data from 1 January 1948 to 31 December 2014. The CPC unified gauge-based precipitation gridded data are developed by combining all applicable data sources available at the NOAA/CPC including ground-based, historical, satellite, and numerical weather information using the optimal interpolation (OI) objective analysis technique (Chen et al., 2008), and thus can be sufficiently reliable for our corroboration and validation.

A2. Validating SHPE's Centroids

Since the distribution of the GHCN-D stations across the United States is not homogeneous, we verify whether any substantial influence associated with the station density might be affecting our findings. To corroborate our results (specifically the spatial distribution of the centroids of SHPEs), we extract the precipitation fields corresponding to 419 SHPEs from the CPC daily U.S. Unified Precipitation data. Two hundred twenty-seven SHPE days were identified within the common record of 1948–2014. We compare the centroids of SHPEs derived from the gridded precipitation product with the centroids detected from the GHCN-D observations as follows.

1. For each grid ($0.25° \times 0.25°$ in the matrix of 300×120) of CPC daily U.S. Unified Precipitation data, we calculate the 99th percentile of the entire precipitation (nonzero) for the 1948–2014 period (24,472 days). The 99th percentile is considered as the extreme threshold for each grid.

2. We take the 227 days identified as SHPE days within the period of 1948–2014 and derive the gridded precipitation map from the CPC daily U.S. Unified Precipitation data.

3. Then, we keep only those grids whose intensities are larger than their corresponding 99th percentile threshold values. We carry on this filtering for all the 227 SHPE-related maps of gridded precipitation data.

4. Next, we calculate the median of longitudes and latitudes of the resulted grids (step 3 above) for each SHPE date. The median will be sufficiently robust against the influence of potential outliers (if any).

5. To calculate the deviation between two centroids (i.e., one from the GHCN-D station-based observations and another from the CPC daily U.S. Unified Precipitation data), the Euclidean distance metric between two centroids (out of 227 pairs) is used:

$$deviation_C = |C_{station} - C_{grid}| = \sqrt{(lon_s - lon_g)^2 + (lat_s - lat_g)^2} \qquad (A1)$$

where C, s, and g refer to the *Centroid*, *station* and *grid*.

6. Ultimately, the summary statistics of $deviation_C$ are estimated (in both degree and geographical distance). The median of $deviation_C$ is 189.65 km. The IQR, mean, and 90th percentile are 227, 270.69, and 530.14 km, respectively.

This experiment demonstrates that the difference between the identified centroids from the GHCN-D observations and the CPC daily U.S. Unified Precipitation data is insignificant (less than ~200 km that can be translated to less than 2° on the ground, which is comparable to the spatial resolution of large-scale atmospheric circulation reanalysis data). We confirmed that the influence of spatial station density across the United States is negligible, and the presented findings and information based on the rain gauges are valid.
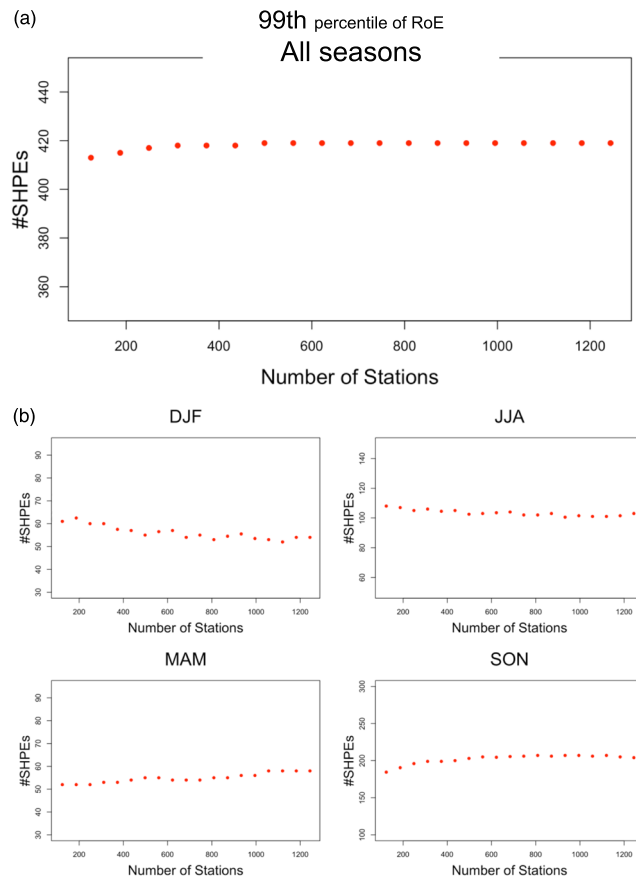

Figure B1. Number of identified SHPEs using different sets of stations across all seasons (a), and separate DJF, MAM, JJA, and SON seasons (b) based on the leave-k%-out test at 99th percentile of the rate of extremes (RoE). The median values are presented across 100 simulations.

Appendix B: Sensitivity to Station Density and RoE Threshold

We designed two experiments to investigate whether there is any systematic influence on the number of identified SHPEs due to limited GHCN-D precipitation stations or the RoE threshold. For instance, how many different SHPEs could be tracked if there were more or less number of rain gages while using the 99th percentile of RoE (used threshold in section 3 above), or different RoE thresholds. These experiments are described below.

B1. Sensitivity of Number of Identified SHPEs to the Number of GHCN-D Stations

Considering the RoE threshold of 99th percentile (as used in section 3 above), we followed a leave-k%-out test, so that each time a certain number of stations from these 1,244 stations are randomly taken out and the remaining stations are used to apply our framework to identify how many SHPEs exist in total, and per season (DJF, MAM, JJA, and SON). We considered k equal to 0 (all 1,244 stations), 5, 10, ..., 85, and 90% of all stations; each time, that many stations will be randomly set aside. Thus, the number of stations that will remain are respectively 1,244, 1,182, 1,120, 1,057, 995, 933, 871, 809, 746, 684, 622, 560, 498, 435, 373, 311, 249, 187, and 124. Then, we calculated RoE across all 115-year daily values (identical to the steps given in section 3 in the paper) and used the 99th percentile of distribution of RoE for each k, followed by counting how many SHPEs exist in total, and per season. We repeat the entire procedure 100 times to account for sampling uncertainty. In Figure B1, we show the results from this test for all the k values against the median number of identified SHPEs across the 100 simulations. There is very little sensitivity of the number of SHPEs to the number of stations. The overall SHPEs remain around 1% of the days, and their seasonal breakdowns are also consistent with what we find based on the 1,244 stations run.

B2. Sensitivity of Number of Identified SHPEs to the Number of GHCN-D Stations and to the RoE Threshold

To investigate if there will be any significant relationship between the number of identified SHPEs and the threshold imposed on RoE, we advance the above experiment using different sets of thresholds for RoE.
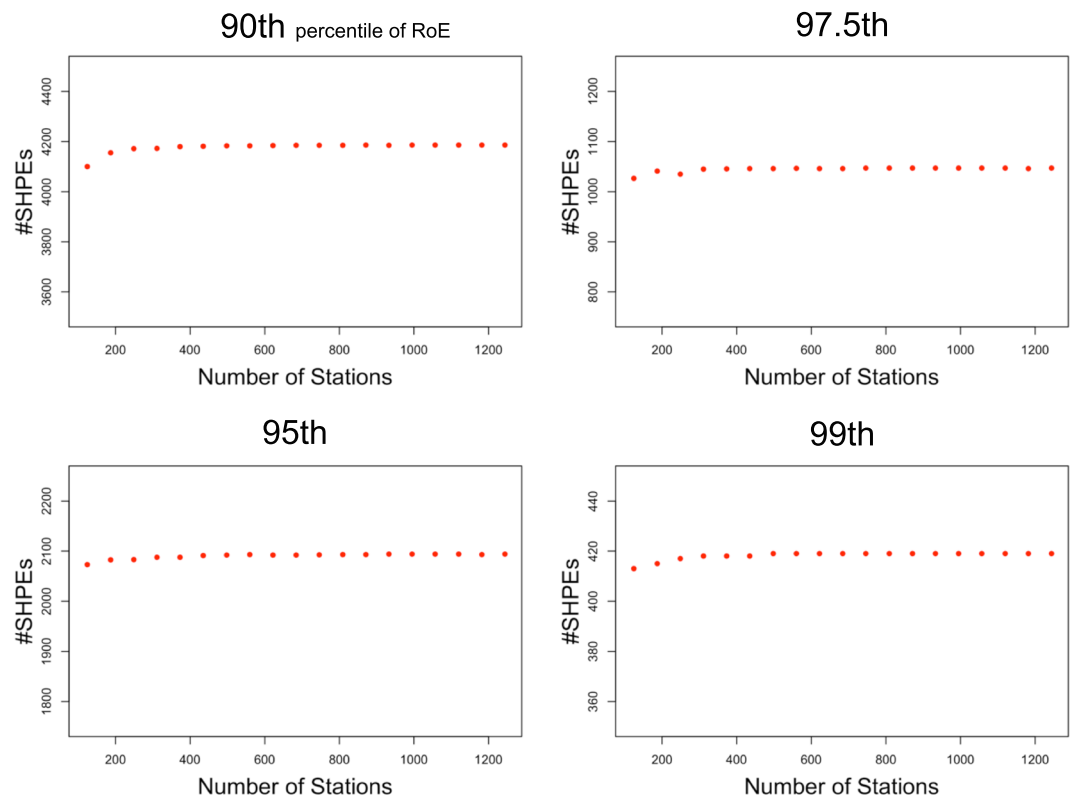

Figure B2. Number of SHPEs that are identified based on different thresholds (90th, 95th, 97.5th, and 99th percentiles) of the rate of extremes (RoE) and varying number of stations.
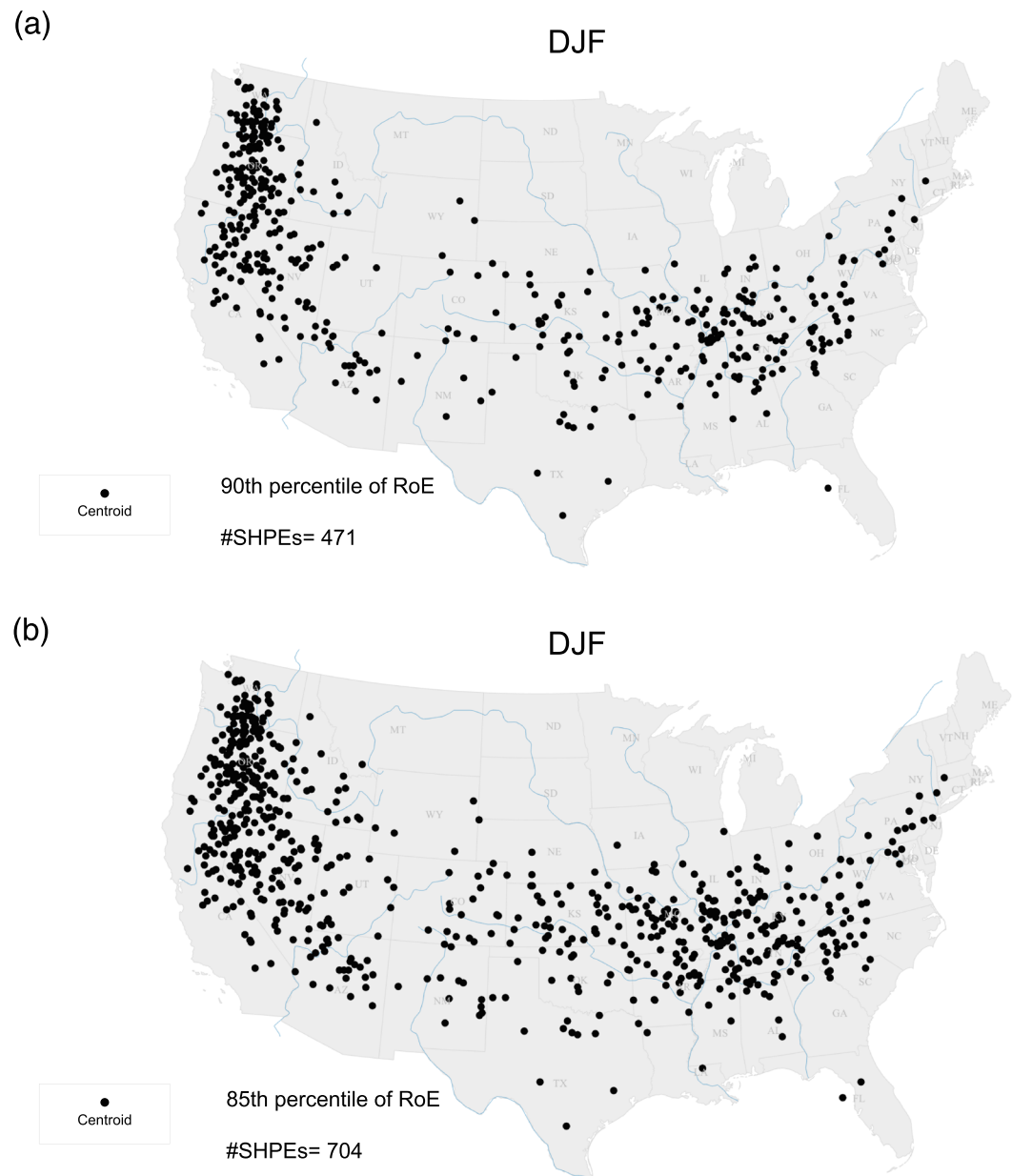
(a)

DJF

Centroid

90th percentile of RoE

#SHPEs= 471

(b)

DJF

Centroid

85th percentile of RoE

#SHPEs= 704

Figure B3. Spatial distribution of the centroids of SHPEs in the DJF season for 90th (a) and 85th (b) percentiles of rate of extremes (RoE). 471 and 704 SHPEs were identified if 90th and 85th percentiles of RoE were selected.

We considered four thresholds — 0.90th, 0.95th, 0.975th, and 0.99th percentiles — of RoE distribution. As before, we repeat the procedure 100 times to account for sampling uncertainty.

The results are presented in Figure B2. As mentioned before, the number of SHPEs that are identified are approximately $(1 - p)\%$, where p is the percentile of the RoE. If we select a 99th percentile, we will approximately get 1% of the days; if we select 90th percentile, we will get approximately 10% of the days. In general, $(1 - p)\%$ of the events show up. It is clear that lowering RoE threshold will allow more spatial events to show up.

In Figure B3, we present the location (centroids) of the SHPEs for the 90th and 85th percentiles threshold on RoE (i.e., $RoE = 0.08$ and 0.067 instead of 0.15 for 99th percentile on RoE). Other events in the DJF season (471 and 704 SHPEs in total in this season) now show up as SHPEs. In general, the density increases as

expected. Note that, with a lower RoE threshold, more SHPEs show up over the coastal areas and California regions.

In conclusion, the two experiments shown above indicate that there will be no bias due to the number of included stations and varying RoE thresholds. Therefore, we can also infer that a higher-resolution data set such as a gridded product will not change the proportion of the identified SHPEs. A lower threshold will yield more events, up to $(1 - p)\%$. Hence, some of the events that are not showing up in the runs that have a 99th percentile on the RoE might show up when that threshold is lowered, and this is an artifact of the percent number of days in the filter (e.g., see Figure B3 for DJF season and 90th or 85th percentiles of RoE). Since our interest was on large-area extents, we selected a 99th percentile RoE.

Conflict of Interest

The authors declare no competing financial interest.

Data Availability Statement

The GHCN-D precipitation data set is available from the NOAA's National Centers for Environmental Information (NCEI) (https://www.ncdc.noaa.gov/ghcnd-data-access). The ERA-20C and ERA-Interim Reanalysis data sets can be accessed through the ECMWF website (https://www.ecmwf.int/en/forecasts/datasets/reanalysis-datasets/era-20c and https://www.ecmwf.int/en/forecasts/datasets/reanalysis-datasets/era-interim). The NCEP/NCAR 20C Reanalysis (V2c) can be downloaded from the NOAA/ESRL/Physical Sciences Laboratory (https://psl.noaa.gov/data/20thC_Rean/); the support for this data set is provided by the U.S. Department of Energy, Office of Science Biological and Environmental Research, and the NOAA's Climate Program Office. The GMTED2010 can be accessed through the U.S. Geological Survey (https://pubs.usgs.gov/of/2011/1073/). The CPC daily U.S. Unified Precipitation data can be downloaded from the NOAA/OAR/ESRL PSD website (https://www.psl.noaa.gov/data/gridded/data.unified.daily.conus.html). The codes relevant to this paper and for replicating the results may be requested from the authors.

References

Agel, L., Barlow, M., Colby, F., Binder, H., Catto, J. L., Hoell, A., & Cohen, J. (2019). Dynamical analysis of extreme precipitation in the US northeast based on large-scale meteorological patterns. *Climate Dynamics*, *52*(3–4), 1739–1760.

AghaKouchak, A., Nasrollahi, N., Li, J., Imam, B., & Sorooshian, S. (2011). Geometrical characterization of precipitation patterns. *Journal of Hydrometeorology*, *12*(2), 274–285.

Akaike, H. (1974). A new look at the statistical model identification. *IEEE Transactions on Automatic Control*, *19*(6), 716–723. https://doi.org/10.1109/tac.1974.1100705

Anders, A. M., Roe, G. H., Hallet, B., Montgomery, D. R., Finnegan, N. J., & Putkonen, J. (2006). Spatial patterns of precipitation and topography in the Himalaya. *Special Papers-Geological Society of America*, *398*, 39.

Arakawa, A. (2006). Atmospheric physics: Scaling tropical rain. *Nature Physics*, *2*(6), 373.

Armal, S., Devineni, N., & Khanbilvardi, R. (2018). Trends in extreme rainfall frequency in the contiguous United States: Attribution to climate change and climate variability modes. *Journal of Climate*, *31*(1), 369–385.

Baldwin, M. E., Kain, J. S., & Lakshmivarahan, S. (2005). Development of an automated classification procedure for rainfall systems. *Monthly weather review*, *133*(4), 844–862.

Bentley, M. L., & Mote, T. L. (1998). A climatology of derecho-producing mesoscale convective systems in the central and eastern United States, 1986–95. part i: Temporal and spatial distribution. *Bulletin of the American Meteorological Society*, *79*(11), 2527–2540.

Berghuijs, W. R., Allen, S. T., Harrigan, S., & Kirchner, J. W. (2019). Growing spatial scales of synchronous river flooding in Europe. *Geophysical Research Letters*, *46*, 1423–1428. https://doi.org/10.1029/2018GL081883

Booth, J. F., Dunn-Sigouin, E., & Pfahl, S. (2017). The relationship between extratropical cyclone steering and blocking along the North American East Coast. *Geophysical Research Letters*, *44*, 11,976–11,984. https://doi.org/10.1002/2017GL075941

Cavazos, T. (1999). Large-scale circulation anomalies conducive to extreme precipitation events and derivation of daily rainfall in northeastern Mexico and southeastern Texas. *Journal of Climate*, *12*(5), 1506–1523.

Chang, W., Stein, M. L., Wang, J., Kotamarthi, V. R., & Moyer, E. J. (2016). Changes in spatiotemporal precipitation patterns in changing climate conditions. *Journal of Climate*, *29*(23), 8355–8376.

Chen, M., Shi, W., Xie, P., Silva, V. B. S., Kousky, V. E., Wayne Higgins, R., & Janowiak, J. E. (2008). Assessing objective techniques for gauge-based analyses of global daily precipitation. *Journal of Geophysical Research*, *113*, D04110. https://doi.org/10.1029/2007JD009132

Clauset, A., Shalizi, C. R., & Newman, M. E. J. (2009). Power-law distributions in empirical data. *SIAM review*, *51*(4), 661–703.

Compo, G. P., Whitaker, J. S., Sardeshmukh, P. D., Matsui, N., Allan, R. J., Yin, X., et al. (2011). The twentieth century reanalysis project. *Quarterly Journal of the Royal Meteorological Society*, *137*(654), 1–28.

Daly, C., Slater, M. E., Roberti, J. A., Laseter, S. H., & Swift Jr, L. W. (2017). High-resolution precipitation mapping in a mountainous watershed: Ground truth for evaluating uncertainty in a national precipitation dataset. *International Journal of Climatology*, *37*, 124–137.

Danielson, J. J., & Gesch, D. B. (2011). Global multi-resolution terrain elevation data 2010 (*GMTED2010*): US Geological Survey.

Dee, D. P., Uppala, S. M., Simmons, A. J., Berrisford, P., Poli, P., Kobayashi, S., et al. (2011). The ERA-Interim reanalysis: Configuration and performance of the data assimilation system. *Quarterly Journal of the royal meteorological society*, *137*(656), 553–597.

Devineni, N., Lall, U., Xi, C., & Ward, P. (2015). Scaling of extreme rainfall areas at a planetary scale. *Chaos: An Interdisciplinary Journal of Nonlinear Science*, *25*(7), 075407.

Dickman, R. (2003). Rain, power laws, and advection. *Physical Review Letters*, *90*(10), 108701.

Dobson, A. J., & Barnett, A. (2008). *An introduction to generalized linear models* (3rd ed.). Boca Raton, FL: Chapman and Hall/CRC.

Dwyer, J. G., & O'Gorman, P. A. (2017). Changing duration and spatial extent of midlatitude precipitation extremes across different climates. *Geophysical Research Letters*, *44*, 5863–5871. https://doi.org/10.1002/2017GL072855

Esteban-Parra, M. J., Rodrigo, F. S., & Castro-Diez, Y. (1998). Spatial and temporal patterns of precipitation in Spain for the period 1880–1992. *International Journal of Climatology*, *18*(14), 1557–1574.

Foufoula-Georgiou, E., & Vuruputur, V. (2001). *Patterns and organization in precipitation* (Chap. 4). Cambridge, UK: Cambridge University Press.

Galewsky, J., & Sobel, A. (2005). Moist dynamics and orographic precipitation in Northern and Central California during the New Years flood of 1997. *Monthly Weather Review*, *133*(6), 1594–1612.

Gelman, A., & Hill, J. (2006). *Data analysis using regression and multilevel/hierarchical models*. New York, NY: Cambridge University Press.

Gershunov, A., Shulgina, T., Ralph, F. M., Lavers, D. A., & Rutz, J. J. (2017). Assessing the climate-scale variability of atmospheric rivers affecting western North America. *Geophysical Research Letters*, *44*, 7900–7908. https://doi.org/10.1002/2017GL074175

Gervais, M., Tremblay, L. B., Gyakum, J. R., & Atallah, E. (2014). Representing extremes in a daily gridded precipitation analysis over the United States: Impacts of station density, resolution, and gridding methods. *Journal of Climate*, *27*(14), 5201–5218.

Gillespie, C. (2015). Fitting heavy tailed distributions: The poweRlaw package. *Journal of Statistical Software*, *64*(2), 1–16.

Guan, B., Waliser, D. E., & Ralph, F. M. (2018). An intercomparison between reanalysis and dropsonde observations of the total water vapor transport in individual atmospheric rivers. *Journal of Hydrometeorology*, *19*(2), 321–337.

Gupta, V. K., & Waymire, E. C. (1993). A statistical analysis of mesoscale rainfall as a random cascade. *Journal of Applied Meteorology*, *32*(2), 251–267.

Hersbach, H., Peubey, C., Simmons, A., Berrisford, P., Poli, P., & Dee, D. (2015). ERA-20CM: A twentieth-century atmospheric model ensemble. *Quarterly Journal of the Royal Meteorological Society*, *141*(691), 2350–2375.

Hitchens, N. M., Baldwin, M. E., & Trapp, R. J. (2012). An object-oriented characterization of extreme precipitation-producing convective systems in the Midwestern United States. *Monthly Weather Review*, *140*(4), 1356–1366.

Huang, X., Swain, D. L., Walton, D. B., Stevenson, S., & Hall, A. D. (2020). Simulating and evaluating atmospheric river induced precipitation extremes along the US Pacific Coast: Case studies from 1980–2017. *Journal of Geophysical Research: Atmospheres*, *125*, e2019JD031554. https://doi.org/10.1029/2019JD031554

Jeon, S., Byna, S., Gu, J., Collins, W. D., & Wehner, M. F. (2015). Characterization of extreme precipitation within atmospheric river events over California. *Advances in Statistical Climatology, Meteorology and Oceanography*, *1*(1), 45.

Jiang, Q. (2003). Moist dynamics and orographic precipitation. *Tellus A: Dynamic Meteorology and Oceanography*, *55*(4), 301–316.

Jiang, Y., Cooley, D., & Wehner, F. M. (2020). Principal component analysis for extremes and application to US precipitation. *Journal of Climate*, *33*(15), 6441–6451.

Johns, R. H. (1982). A synoptic climatology of northwest flow severe weather outbreaks. Part I: Nature and significance. *Monthly Weather Review*, *110*(11), 1653–1663.

Johns, R. H. (1993). Meteorological conditions associated with bow echo development in convective storms. *Weather and Forecasting*, *8*(2), 294–299.

Kansakar, S. R., Hannah, D. M., Gerrard, J., & Rees, G. (2004). Spatial pattern in the precipitation regime of Nepal. *International Journal of Climatology: A Journal of the Royal Meteorological Society*, *24*(13), 1645–1659.

Khouakhi, A., & Villarini, G. (2016). On the relationship between atmospheric rivers and high sea water levels along the US West Coast. *Geophysical Research Letters*, *43*, 8815–8822. https://doi.org/10.1002/2016GL070086

Kunkel, K. E., & Champion, S. M. (2019). An assessment of rainfall from Hurricanes Harvey and Florence relative to other extremely wet storms in the United States. *Geophysical Research Letters*, *46*, 13,500–13,506. https://doi.org/10.1029/2019GL085034

Kunkel, K. E., Easterling, D. R., Kristovich, D. A. R., Gleason, B., Stoecker, L., & Smith, R. (2012). Meteorological causes of the secular variations in observed extreme precipitation events for the conterminous United States. *Journal of Hydrometeorology*, *13*(3), 1131–1141.

Kunkel, K. E., Karl, T. R., Squires, M. F., Yin, X., Stegall, S. T., & Easterling, D. R. (2020). Precipitation extremes: Trends and relationships with average precipitation and precipitable water in the contiguous United States. *Journal of Applied Meteorology and Climatology*, *59*(1), 125–142.

Kunkel, K. E., Stevens, S. E., Stevens, L. E., & Karl, T. R. (2019). Observed climatological relationships of extreme daily precipitation events with precipitable water and vertical velocity in the contiguous United States. *Geophysical Research Letters*, *47*, e2019GL086721. https://doi.org/10.1029/2019GL086721

Larson, L. W. (1997). The great USA flood of 1993. *IAHS Publications-Series of Proceedings and Reports-Intern Assoc Hydrological Sciences*, *239*, 13–20.

Lavers, D. A., & Villarini, G. (2013). Atmospheric rivers and flooding over the central United States. *Journal of Climate*, *26*(20), 7829–7836.

Lavers, D. A., & Villarini, G. (2015). The contribution of atmospheric rivers to precipitation in Europe and the United States. *Journal of Hydrology*, *522*, 382–390.

Leung, L. R., Qian, Y., Bian, X., & Hunt, A. (2003). Hydroclimate of the western United States based on observations and regional climate simulation of 1981–2000. Part II: Mesoscale ENSO anomalies. *Journal of Climate*, *16*(12), 1912–1928.

Liu, B., Tan, X., Gan, T. Y., Chen, X., Lin, K., Lu, M., & Liu, Z. (2020). Global atmospheric moisture transport associated with precipitation extremes: Mechanisms and climate change impacts. *Wiley Interdisciplinary Reviews: Water*, *7*(2), e1412.

Loader, C. (2006). *Local regression and likelihood*. New York, NY: Springer Science & Business Media.

Loikith, P. C., Lintner, B. R., & Sweeney, A. (2017). Characterizing large-scale meteorological patterns and associated temperature and precipitation extremes over the northwestern United States using self-organizing maps. *Journal of Climate*, *30*(8), 2829–2847.

Lovejoy, S. (1982). Area-perimeter relation for rain and cloud areas. *Science*, *216*(4542), 185–187.

Lu, M., & Hao, X. (2017). Diagnosis of the tropical moisture exports to the mid-latitudes and the role of atmospheric steering in the extreme precipitation. *Atmosphere*, *8*(12), 256.

Lu, M., Tippett, M., & Lall, U. (2015). Changes in the seasonality of tornado and favorable genesis conditions in the central United States. *Geophysical Research Letters*, *42*, 4224–4231. https://doi.org/10.1002/2015GL063968

Mahoney, K., Jackson, D. L., Neiman, P., Hughes, M., Darby, L., Wick, G., et al. (2016). Understanding the role of atmospheric rivers in heavy precipitation in the southeast United States. *Monthly Weather Review*, *144*(4), 1617–1632.

Mann, H. B. (1945). Nonparametric tests against trend. *Econometrica: Journal of the Econometric Society*, *13*(3), 245–259.

Marquardt Collow, A. B., Bosilovich, M. G., & Koster, R. D. (2016). Large-scale influences on summertime extreme precipitation in the northeastern United States. *Journal of Hydrometeorology*, *17*(12), 3045–3061.

Mason, S. J., Waylen, P. R., Mimmack, G. M., Rajaratnam, B., & Harrison, J. M. (1999). Changes in extreme rainfall events in South Africa. *Climatic Change*, *41*(2), 249–257.

Menne, M. J., Durre, I., Vose, R. S., Gleason, B. E., & Houston, T. G. (2012). An overview of the global historical climatology network-daily database. *Journal of Atmospheric and Oceanic Technology*, *29*(7), 897–910.

Milrad, S. M., Atallah, E. H., & Gyakum, J. R. (2010). Synoptic typing of extreme cool-season precipitation events at St. John's, Newfoundland, 1979–2005. *Weather and Forecasting*, *25*(2), 562–586.

Mo, K. C., Nogues-Paegle, J., & Paegle, J. (1995). Physical mechanisms of the 1993 summer floods. *Journal of the Atmospheric Sciences*, *52*(7), 879–895.

NOAA/NCDC (2017). NOAA National Climatic Data Center. NOAA National Centers for Environmental Information. Available online: https://www.ncdc.noaa.gov/ (accessed on 01 September 2017).

NOAA/NCEI (2019). U.S. billion-dollar weather and climate disasters. NOAA National Centers for Environmental Information. Available online: https://www.ncdc.noaa.gov/billions/ (accessed on 01 February 2019).

Mondal, S., Mishra, A. K., & Leung, L. R. (2020). Spatiotemporal characteristics and propagation of summer extreme precipitation events over USA: A complex network analysis. *Geophysical Research Letters*, *47*, e2020GL088185. https://doi.org/10.1029/2020GL088185

Najibi, N., Devineni, N., Lu, M., & Perdigão, R. A. P. (2019). Coupled flow accumulation and atmospheric blocking govern flood duration. *npj Climate and Atmospheric Science*, *2*(1), 19.

Nakamura, J., Lall, U., Kushnir, Y., Robertson, A. W., & Seager, R. (2013). Dynamical structure of extreme floods in the US Midwest and the United Kingdom. *Journal of Hydrometeorology*, *14*(2), 485–504.

Neiman, P. J., Ralph, F. M., Wick, G. A., Lundquist, J. D., & Dettinger, M. D. (2008). Meteorological characteristics and overland precipitation impacts of atmospheric rivers affecting the West Coast of North America based on eight years of SSM/I satellite observations. *Journal of Hydrometeorology*, *9*(1), 22–47.

Newman, M. E. J. (2005). Power laws, Pareto distributions and Zipf's law. *Contemporary physics*, *46*(5), 323–351.

Pan, M., & Lu, M. (2019). A novel atmospheric river identification algorithm. *Water Resources Research*, *55*, 6069–6087. https://doi.org/10.1029/2018WR024407

Pandey, G. R., Cayan, D. R., & Georgakakos, K. P. (1999). Precipitation structure in the Sierra Nevada of California during winter. *Journal of Geophysical Research*, *104*(D10), 12,019–12,030.

Peñarrocha, D., Estrela, M. J., & Millán, M. (2002). Classification of daily rainfall patterns in a Mediterranean area with extreme intensity levels: The Valencia region. *International Journal of Climatology*, *22*(6), 677–695.

Pfahl, S., & Wernli, H. (2012). Quantifying the relevance of atmospheric blocking for co-located temperature extremes in the Northern Hemisphere on (sub-) daily time scales. *Geophysical Research Letters*, *39*, L12807. https://doi.org/10.1029/2012GL052261

Rajagopalan, B., & Tarboton, D. G. (1993). Understanding complexity in the structure of rainfall. *Fractals*, *1*(03), 606–616.

Ralph, F. M., Rutz, J. J., Cordeira, J. M., Dettinger, M., Anderson, M., Reynolds, D., et al. (2019). A scale to characterize the strength and impacts of atmospheric rivers. *Bulletin of the American Meteorological Society*, *100*(2), 269–289.

Ricks, R. J., Trotter, P., Johnson, G., Revitte, F., Guiney, J., Pfost, R., & Reed, D. (1997). The historic southeast Louisiana and southern Mississippi flood of May 8–10, 1995. NOAA/NWS/SRHQ. Retrieved from http://www.srh.noaa.gov/ssd/techmemo/sr183.htm

Risser, M. D., Paciorek, C. J., Wehner, M. F., O'Brien, T. A., & Collins, W. D. (2019). A probabilistic gridded product for daily precipitation extremes over the United States. *Climate Dynamics*, *53*(5–6), 2517–2538.

Sapozhnikov, V. B., & Foufoula-Georgiou, E. (2007). An exponential Langevin-type model for rainfall exhibiting spatial and temporal scaling, *Nonlinear dynamics in geosciences* (pp. 87–100). Springer.

Schertzer, D., & Lovejoy, S. (1987). Physical modeling and analysis of rain and clouds by anisotropic scaling multiplicative processes. *Journal of Geophysical Research*, *92*(D8), 9693–9714.

Smith, B. T., Castellanos, T. E., Winters, A. C., Mead, C. M., Dean, A. R., & Thompson, R. L. (2013). Measured severe convective wind climatology and associated convective modes of thunderstorms in the contiguous United States, 2003–09. *Weather and Forecasting*, *28*(1), 229–236.

Smith, B. T., Thompson, R. L., Grams, J. S., Broyles, C., & Brooks, H. E. (2012). Convective modes for significant severe thunderstorms in the contiguous United States. Part I: Storm classification and climatology. *Weather and Forecasting*, *27*(5), 1114–1135.

Steinschneider, S., & Lall, U. (2015). Daily precipitation and tropical moisture exports across the eastern United States: An application of archetypal analysis to identify spatiotemporal structure. *Journal of Climate*, *28*(21), 8585–8602.

Tabony, R. C. (1981). A principal component and spectral analysis of European rainfall. *Journal of Climatology*, *1*(3), 283–294.

Timmermans, B., Wehner, M., Cooley, D., O'Brien, T., & Krishnan, H. (2019). An evaluation of the consistency of extremes in gridded precipitation data sets. *Climate Dynamics*, *52*(11), 6651–6670.

Touma, D., Michalak, A. M., Swain, D. L., & Diffenbaugh, N. S. (2018). Characterizing the spatial scales of extreme daily precipitation in the United States. *Journal of Climate*, *31*(19), 8023–8037.

Trapp, R. J., Tessendorf, S. A., Godfrey, E. S., & Brooks, H. E. (2005). Tornadoes from squall lines and bow echoes. Part I: Climatological distribution. *Weather and Forecasting*, *20*(1), 23–34.

Turnipseed, D. P., Baldwin, W. T., Cooper, L. M., & Floyd, P. C. (1995). Flooding in coastal areas of Mississippi and southeastern Louisiana, May 9–10, 1995. US Geological Survey. Retrieved from https://pubs.er.usgs.gov/publication/fs15595

US/Census/Bureau (2012). U.S. population and housing unit counts. 2010 Census of Population and Housing. Available online: https://www.census.gov/prod/cen2010/cph-2-1.pdf (accessed on 01 September 2018).

Vatti, M., Remata, S. R., & Chigbu, P. (2003). Simulations of the historic southeast Louisiana and southern Mississippi flood activity during May 8–10th, 1995 to build a prototype GIS/RS based ERAISA for gulf coastal states of the United States, *IGARSS 2003 IEEE International Geoscience and Remote Sensing Symposium. Proceedings* (Vol. 4, pp. 2520–2522).

Voskresenskaya, E., & Vyshkvarkova, E. (2016). Extreme precipitation over the Crimean Peninsula. *Quaternary International*, *409*, 75–80.

Waliser, D., & Guan, B. (2017). Extreme winds and precipitation during landfall of atmospheric rivers. *Nature Geoscience*, *10*(3), 179.

Wang, S.-Y., & Chen, T.-C. (2009). The late-spring maximum of rainfall over the US Central Plains and the role of the low-level jet. *Journal of Climate*, *22*(17), 4696–4709.

Wang, S.-Y., Chen, T.-C., & Correia, J. (2011). Climatology of summer midtropospheric perturbations in the US Northern Plains. Part I: Influence on northwest flow severe weather outbreaks. *Climate Dynamics*, *36*(3–4), 793–810.

Wang, S.-Y., Davies, R. E., & Gillies, R. R. (2013). Identification of extreme precipitation threat across midlatitude regions based on short-wave circulations. *Journal of Geophysical Research: Atmospheres*, *118*, 11–059. https://doi.org/10.1002/jgrd.50841

Wasko, C., Sharma, A., & Westra, S. (2016). Reduced spatial extent of extreme storms at higher temperatures. *Geophysical Research Letters*, *43*, 4026–4032. https://doi.org/10.1002/2016GL068509

Weaver, S. J., & Nigam, S. (2008). Variability of the Great Plains low-level jet: Large-scale circulation context and hydroclimate impacts. *Journal of Climate*, *21*(7), 1532–1551.

Wold, S., Esbensen, K., & Geladi, P. (1987). Principal component analysis. *Chemometrics and Intelligent Laboratory Systems*, *2*(1–3), 37–52.

Xie, P., Chen, M., Yang, S., Yatagai, A., Hayasaka, T., Fukushima, Y., & Liu, C. (2007). A gauge-based analysis of daily precipitation over East Asia. *Journal of Hydrometeorology*, *8*(3), 607–626.

Zepeda-Arce, J., Foufoula-Georgiou, E., & Droegemeier, K. K. (2000). Space-time rainfall organization and its role in validating quantitative precipitation forecasts. *Journal of Geophysical Research*, *105*(D8), 10,129–10,146.

Zhang, X., Hogg, W. D., & Mekis, E. (2001). Spatial and temporal characteristics of heavy precipitation events over Canada. *Journal of Climate*, *14*(9), 1923–1936.

Zhang, W., & Villarini, G. (2018). Uncovering the role of the East Asian jet stream and heterogeneities in atmospheric rivers affecting the western United States. *Proceedings of the National Academy of Sciences*, *115*(5), 891–896.